Key Points:
- Surface processes enhance plastic strain localization
- Surface processes provide important feedback on rifted margin structure
- Normal faults distribution, margins width, time of crustal breakup, and stratigraphic records are controlled by these feedbacks

Correspondence to:
T. Theunissen,
thomas.theunissen@geo.uib.no

Long-Term Coupling and Feedback Between Tectonics and Surface Processes During Non-Volcanic Rifted Margin Formation

Thomas Theunissen[1] and **Ritske S. Huismans[1]**

[1]Department of Earth Science, University of Bergen, Bergen, Norway

Abstract Here we present high-resolution 2-D coupled tectonic-surface processes modeling of extensional basin formation. We focus on understanding feedbacks between erosion and deposition and tectonics during rift and passive margin formation. We test the combined effects of crustal rheology and varying surface process efficiency on structural style of rift and passive margin formation. The forward models presented here allow to identify the following four feedback relations between surface processes and tectonic deformation during rifted margin formation. (1) Erosion and deposition promote strain localization and enhance large offset asymmetric normal fault growth. (2) Progressive infill from proximal to more distal half grabens promotes the formation of synthetic sets of basinward dipping normal faults for intermediate crustal strength cases. (3) Sediment loading on top of undeformed crustal rafts in weak crust cases enhances middle and lower crustal flow resulting in sag basin subsidence. (4) Interaction of high sediment supply to the distal margin in very weak crust cases results in detachment-based rollover sedimentary basins. Our models further show that erosion efficiency and drainage area provide a first-order control on sediment supply during rifting where rift-related topography is relatively quickly eroded. Long-term sustained sediment supply to the rift basins requires elevated onshore drainage basins. We discuss similar variations in structural style observed in natural systems and compare them with the feedbacks identified here.

1. Introduction

The morphology and structure of rifted passive margins are characterized by a high variability in width, fault geometry, and nature and geometry of the sedimentary succession (Clerc et al., 2017). Studies of active rifts and extensional domains show that their internal structure, history, and dimensions are highly variable (Ruppel, 1995). Contrasting narrow, wide, and core complex modes of extension are predicted to depend on crustal thickness, geotherm, and strain rate (Buck, 1991). Forward numerical models demonstrate the control of rheological stratification, with two end-members types for varying crustal strength: strong crust resulting in narrow rifts with few high angle normal faults (Type 1) and weak crust resulting in wide rifted margins with significant middle/lower crustal flow and core complex style deformation (Type 2; e.g., Huismans & Beaumont, 2011, 2014; Svartman Dias et al., 2015). Many aspects of rifts system remain unexplained owing to the complexity of the processes that interact with one another. Weakening processes and structural and rheological inheritance of the lithosphere play an important role in controlling the structural style of deformation (e.g., Brune et al., 2014; Duretz et al., 2016; Huismans & Beaumont, 2002, 2003; Lavier & Manatschal, 2006; Salazar-Mora et al., 2018; Wu & Lavier, ; Wu et al., 2015). In this study we focus on the role of surface processes during nonvolcanic rifted passive margin formation.

Coupling and feedback between surface processes and tectonics during extension have received less attention than in orogenic systems (e.g., Avouac & Burov, 1996; Beaumont et al., 1992; Beaumont et al., 2001; Erdős et al., 2014; Stolar et al., 2006; Thieulot et al., 2014; Whipple, 2009; Willett, 1999). Previous studies have focused on the erosion of great escarpments and postrift deposition and consequences for flexural isostatic rebound (Braun et al., 2013; Braun & van der Beek, 2004; Brown et al., 2002; Sacek et al., 2012; van Balen et al., 1995; van der Beek et al., 2002). The syn-rift sedimentary basin fill is often seen as a result of the interaction between sediment supply, fault-controlled subsidence, and sea level fluctuations (e.g., Gawthorpe et al., 1994; Leeder & Gawthorpe, 1987; Schlische, 1991; Prosser, 1993).

A range of studies have explored the coupling and feedback between surface processes and fault activity. On short seismic time scales, erosional unloading may contribute to Coulomb stress loading along thrust fault

planes leading to increased fault activity (Steer et al., 2014). On long-term tectonic time scales, displacement on a single normal fault is enhanced by footwall erosion and hanging wall deposition (Maniatis et al., 2009). Olive et al. (2014) argue that the life span of normal faults is increased in response to surface processes resulting in large fault offsets. Several studies (Buiter et al., 2008; Choi et al., 2013; Olive et al., 2014) indicate that syntectonic erosion and deposition control location and geometry of secondary faults and delay fault migration. Strak et al. (2011) using analog models show that throw rate controls fluvial incision. Similarly, several recent studies have investigated the sensitivity of landscape evolution to normal fault activity (e.g., Demoulin et al., 2018; Petit et al., 2009; Roda-Boluda & Whittaker, 2018).

Several previous studies explore the interaction and feedback of surface processes and extensional tectonics at the scale of the whole rifted margin system. Bialas and Buck (2009) show using forward numerical modeling with simple sediment aggradation that sedimentation may promote narrow rifting. In contrast, Burov & Poliakov (2001, 2003) using coupled forward models show that increased surface processes efficiency may enhance distributed deformation (higher crustal thinning and wider margins), while they suggested that erosion of rift flanks in combination with high sedimentation rate in the rift basin induces outward lower crustal flow toward the rift flanks. Andrés-Martínez et al. (2019) show using 2-D coupled forward models with a surface diffusion model for erosion and sedimentation that surface processes enhance strain localization and control margin width and symmetry. High sedimentation rate favors abrupt crustal necking and narrow proximal margins. Efficient mass transport to the distal margin by subaerial processes (low sea level) leads to more symmetric and narrower conjugate margins.

Here we use a high-resolution 2-D thermo-mechanical numerical model (Erdős et al., 2014; Thieulot, 2011) coupled with a mass balancing fluvial erosion, marine deltaic deposition model to investigate the effect of varying rheological conditions, surface process efficiency, and sea level on the structural style of rift and passive margin formation. We first present the numerical modeling approach followed by the model results. We discuss primary feedback relations from the model results and compare these with observations from natural rift systems.

2. Modeling Approach

We use an arbitrary Lagrangian-Eulerian finite element method for the solution of thermo-mechanical coupled, plane strain, incompressible viscous-plastic creeping flows (Thieulot, 2011; Erdős et al., 2014). The finite element model solves the force balance equations of equilibrium for quasi-static incompressible flows in two dimensions:

$$\nabla(\mu_{\text{eff}}\nabla v) + \lambda\nabla(\nabla{\cdot}v) + \rho g = 0, \tag{1}$$

where μ_{eff} is the effective viscosity, v is the velocity, ρ the density, and g the gravity acceleration. In equation (1), mass conservation equation with incompressibility constraint ($\nabla v + \frac{p}{\lambda} = 0$ where p is the pressure and λ a penalty parameter with same dimension as a bulk viscosity) and momentum conservation equation (Stokes equation) are combined (Thieulot, 2011). In addition to the mechanical system, we also solve the thermal evolution in two dimensions using the finite element method:

$$\rho c_p\left(\frac{\partial T}{\partial t} + v\nabla T\right) = \nabla(k\nabla T) + H + v_z\alpha_T gT\rho. \tag{2}$$

Here T is the temperature, c_p is the specific heat capacity, k the thermal conductivity, and H the radiogenic heat production. The last term in the heat balance equation is the temperature correction for adiabatic heating and cooling when material moves vertically at velocity v_z, where α_T represents the volumetric thermal expansion coefficient.

When the state of stress is below the frictional-plastic yield stress, the flow is viscous and is specified by temperature-dependent nonlinear power law rheologies based on laboratory measurements on "wet" quartz (Gleason & Tullis, 1995) and "wet" olivine (Karato & Wu, 1993). The effective viscosity, μ_{eff}, in the power law rheology is of the general form:

Table 1
Parameters for the Lithosphere-Scale Thermo-Mechanical Models

Parameter	Symbol	Units	Sediments	Upper crust (0–25 km)	Lower crust (25–35 km)	Lithopheric mantle	Sublithospheric mantle
			Rheological parameters				
Effective viscosity range	μ_{eff}	Pa.s	10^{18}–10^{27}	10^{18}–10^{27}	10^{18}–10^{27}	10^{18}–10^{27}	10^{18}–10^{27}
Angle of internal friction	ϕ_{eff}	°	15	15	15	15	15
→ after strain weakening	ϕ_{eff}	°	2	2	2	2	2
Initial cohesion	C	MPa	10	20	20	20	20
→ after strain weakening	C	MPa	4	4	4	4	4
Strain weakening range	—	—			0.05–1.05		
Flow law	—	—	WQtz[a]	WQtz[a]	WQtz[a]	WO[b]	WO[b]
Scaling factor (f)	—	—	1		30; 1; 0.1 ;0.02	5	1
Power law exponent	n	—	4	4	4	3	3
Activation energy	Q	kJ/mol	222.81	222.81	222.81	429.83	429.83
Constant	A	Pa^{-n} s^{-1}	$8.574 \cdot 10^{-28}$		$8.574 \cdot 10^{-28}$	$1.758 \cdot 10^{-14}$	$1.758 \cdot 10^{-14}$
Activation volume	V	m^3/s	0.0	0.0	0.0	$15 \cdot 10^{-6}$	$15 \cdot 10^{-6}$
Density at T_0= 273 K	ρ_0	kg/m^3	1,802–2,640[c]	2,750	2,900	3,300	3,300
			Thermal parameters				
Thermal conductivity	k	W·m^{-1}·K^{-1}	2.25	2.25	2.25	2.25	2.25–51.46
Heat capacity	c_p	J·K^{-1}·kg^{-1}	818.18	818.18	775.86	681.81	681.81
Thermal diffusivity [d]	η	m^2/s	$1.0 \cdot 10^{-6}$	$1.0 \cdot 10^{-6}$	$1.0 \cdot 10^{-6}$	$1.0 \cdot 10^{-6}$	1.0–$22.9 \cdot 10^{-6}$
Heat production rate	H	W/m^3	$1.196 \cdot 10^{-6}$	$1.196 \cdot 10^{-6}$	$0.483 \cdot 10^{-6}$	0	0
Thermal expansion coefficient	α_T	K^{-1}	$3.1 \cdot 10^{-5}$	$3.1 \cdot 10^{-5}$	$3.1 \cdot 10^{-5}$	$3.1 \cdot 10^{-5}$	$3.1 \cdot 10^{-5}$
			Boundary conditions				
Surface temperature	T_{surf}	°C		0			
Initial prerift sediments thickness	$h_{\mathrm{pre\text{-}sed}}$	km		3			
Initial moho depth	d_{moho}	km		35			
Moho temperature	T_{moho}	°C		550			
LAB depth	d_{LAB}	km		120			
LAB temperature	T_{LAB}	°C		1,328			
Basal lower mantle temperature	T_{LM}	°C		1,520			
Extension velocity	V_{ext}	cm/year		1			

Note. Flow laws are based on power law with creep parameters from WQtz (Gleason & Tullis, 1995) and WO (Karato & Wu, 1993). Values are given with two digits precision. WQtz = wet quartz; WO = wet olivine; LAB = Lithosphere-Astenosphere Boundary. [a]Dislocation creep models for WQtz. [b]Dislocation creep models for WO. [c]Sediment compaction (see Supporting Information S1). [d]$\eta = k/\rho C_p$.

$$\mu_{\mathrm{eff}} = fA^{-1/n}\dot{E}_2^{(1-n)/2n}exp\left(\frac{Q+Vp}{nRT}\right), \tag{3}$$

where $\dot{E}_2$ is the second invariant of the deviatoric strain rate tensor $\frac{1}{2}\dot{\varepsilon}_{ij}\dot{\varepsilon}_{ij}$, A is the preexponential scaling factor, n is the power law exponent, Q is the activation energy, R is the universal gas constant, and V is the activation volume. The factor f is used to scale viscosities calculated from the reference quartz and olivine flow laws, thereby producing strong and weak versions of these materials. Frictional-plastic yielding is modeled with a pressure-dependent Drucker-Prager yield criterion which is equivalent to the Coulomb yield criterion for incompressible deformation in plane strain. Yielding occurs when

$$\sigma_y = \sqrt{J_2} = C\cos(\phi_{\mathrm{eff}}) + p\sin(\phi_{\mathrm{eff}}), \tag{4}$$

where J_2 is the second invariant of the deviatoric stress $\frac{1}{2}\tau_{ij}\tau_{ij}$, l$\tau_{ij}$ is the deviatoric stress tensor, ϕ_{eff} is the effective internal angle of friction, $p\sin(\phi_{\mathrm{eff}})=(p-p_f)\sin(\phi)$, p_f is the pore-fluid pressure, and C is the cohesion. With appropriate choices of C and ϕ_{eff}, this yield criterion can approximate frictional sliding in rocks and the effect of pore-fluid pressures. Plastic flow is incompressible. Strain softening is introduced by a linear decrease of $\phi_{\mathrm{eff}}(\varepsilon)$ from 15° to 2° and $C(\varepsilon)$ from 20 to 4 MPa with respect to plastic strain (ε; Table 1; Buck,
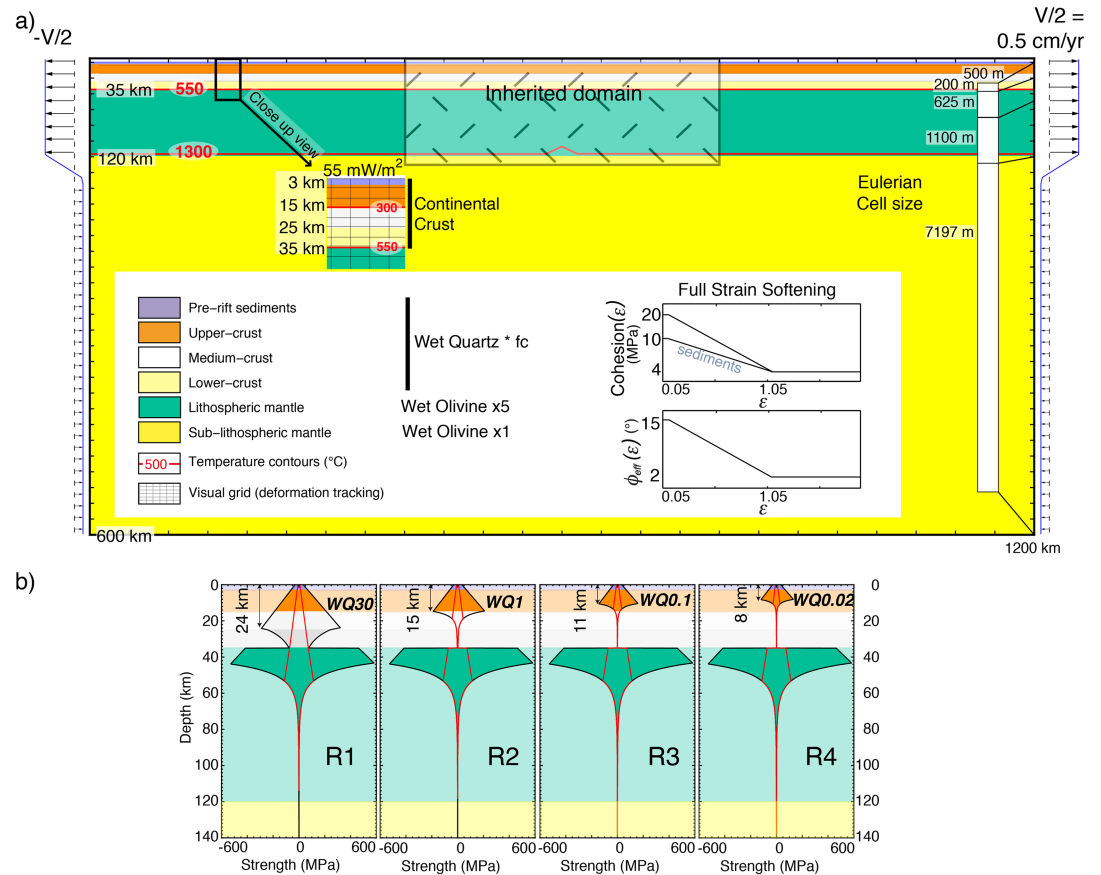
Figure 1. Model setup. (a) Model geometry showing rheological-layered structure, position, and size of the inherited domain (see Supporting Information S1), boundary conditions, initial thermal state, and frictional-plastic strain softening. All values used for the mechanical and thermal parameters are listed in Table 1. (b) Strength profiles for the four representative crustal rheologies. The yield strength envelopes are constructed using a strain rate of $2.6 \cdot 10^{-16}\,\text{s}^{-1}$ that corresponds to the strain rate over the full width of the model (1,200 km) at 10 mm/year.

1993; Huismans & Beaumont, 2002; Lavier et al., 1999, 2000; Figure 1). The plastic strain is updated at every time step with the second invariant of the deviatoric strain. The incompressible plastic flow becomes equivalent to a viscous flow if an effective viscosity, μ_{eff}^{p}, for a plastic material is defined such that $\mu_{\text{eff}}^{p} = \sqrt{J_2} / \sqrt{\dot{E}_2}$. Setting the viscosity to μ_{eff}^{p} in regions that are on frictional-plastic yield satisfies the yield condition and allows the velocity field to be determined from the finite element solution of equation (1). The overall nonlinear solution is determined iteratively using $\mu = \mu_{\text{eff}}^{p}$ (for regions of plastic flow) and $\mu = \mu_{\text{eff}}^{v}$ (for regions of viscous flow; Willett, 1992).

The mechanical and thermal evolution are coupled through the temperature dependence of viscosity and density and are solved alternately during each time step. Densities of crust and mantle depend on temperature with $\rho(T) = \rho_0(1 - \alpha(T - T_0))$, where α is the coefficient of thermal expansion and ρ_0 is the density at $T = T_0$. Parameters are given in Table 1 and in the Supporting Information S1

2.1. Model Setup and Boundary Conditions

The models are set up as an idealized rheologically layered lithosphere above a sublithospheric mantle in a 600-km-high and 1,200-km-wide model domain (Figure 1). The lithosphere consists of a 35-km-thick crust and 85-km mantle lithosphere overlying the sublithospheric mantle. The top 3 km of the crust represents prerift sediments with the same rheology as the upper crust.

The Eulerian grid consists of 2,400 and 290 elements in the horizontal and vertical directions, respectively. The distribution of the elements is irregular in the vertical direction, allowing for high resolution in the upper crust with a vertical resolution of Δz=200 m in the first 20 km, Δz=625 m between 20 and 70 km, Δz=1,100 m between 70 and 120 km, and Δz=7,917 m between 120 and 600 km. The resolution in the horizontal direction is 500 m for the entire model domain.

Extensional horizontal velocity boundary conditions (v = ±0.5 cm/year) are applied to the lithosphere, and the corresponding exit flux is balanced by a low velocity inflow in the sublithospheric mantle. The top of the model is a free surface. The sides and base are vertical and horizontal free slip boundaries, respectively (Figure 1a).

Thermal boundary conditions are specified basal temperature, 1,520 °C, and insulated lateral boundaries. The initial temperature field is laterally uniform and increases with depth from the surface (T_0=0 °C) to the base of the crust (initial Moho temperature, Tm=550 °C) with a surface heat flux of 55.3 mW/m^2. Below the Moho, temperature linearly decreases to the base of mantle lithosphere (initially at T = 1,328 °C); the temperature of the sublithospheric mantle follows an adiabatic gradient (0.4 °C/km). Thermal conductivity linearly increases to 51.46 W·m^{-1}·K^{-1} at 1,350 °C (~125-km depth), corresponding to scaling the thermal conductivity by the Nusselt number of upper mantle convection. The enhanced conductivity maintains a nearly constant heat flux to the lithosphere base and an adiabatic temperature gradient in the sublithospheric mantle (e.g., Pysklywec & Beaumont, 2004).

2.2. Rheological Setup

The crust follows a wet quartz rheology (Gleason & Tullis, 1995) with different scaling factors as a way to test the effect of varying crustal strength (Figure 1). We test four contrasting crustal rheologies, varying scaling factor f_{uc} from 30, 1, 0.1, and 0.02, resulting in thickness of the frictional-plastic upper crust that ranges from 25 km to about 8 km. The viscosity scaling (Figure 1) represents a simple technique that creates either strong crust or weak viscous crust without recourse to additional flow laws, each with its own uncertainties. The scaling can either be interpreted as a measure of the uncertainty in the flow properties of rocks where flow is dominated by quartz (e.g., wet or dry) or taken to represent variations in thermal state and composition (e.g., Huismans & Beaumont, 2011, 2014).

We investigate systems that are characterized by mechanical heterogeneity represented by white noise in the initial strain field (Figures 1 and S1). This approach is designed to represent inheritance of deformation from previous tectonic phases. Specifically, the plastic strain (ϵ) is initialized with white noise that has a Gaussian distribution with a mean value set to 0.3 and with a maximum value 0.8. Inherited weakness is provided by a tapered symmetrical 400-km-wide area in the model center. A small thermal heterogeneity is introduced at the base of the lithosphere in the model center in order to enhance rift localization (see Supporting Information S1 for a detailed description). The orientation of faults and thus the asymmetry of the developing rift is not prescribed and is generated spontaneously.

In order to ensure mass conservation, the average pressure at the bottom part of the model is maintained constant by adjusting the influx of the sublithospheric mantle at the sides. This allows defining an absolute sea level within the model independent from surface displacement. Based on sea level, a water load is implemented in order to fully consider all mass loads on the free surface.

2.3. Surface Processes Modeling

Surface processes in the forward model act on the free upper surface (Figure 2). We implement mass balancing erosion and deposition. A river profile is applied to topography above sea level between each local minimum and maximum similarly to previous studies (e.g., Steer et al., 2011; Willett, 1999, 2010). Transported sediment can be deposited along a river profile and in lakes above sea level, by deltaic progradation below sea level, or leave the model domain when it reaches the sides. Instantaneous mechanical compaction due to vertical loading of sediments is included with an associated volume and density change (see Supporting Information S1 for detailed description; Albertz & Ings, 2012; Athy, 1930; Chamot-Rooke et al., 1999; Cowie & Karner, 1990; Goteti et al., 2012; Tenzer & Gladkikh, 2014). The change in free-surface topography is a result of the net effect of tectonic uplift or subsidence, erosion, and deposition:
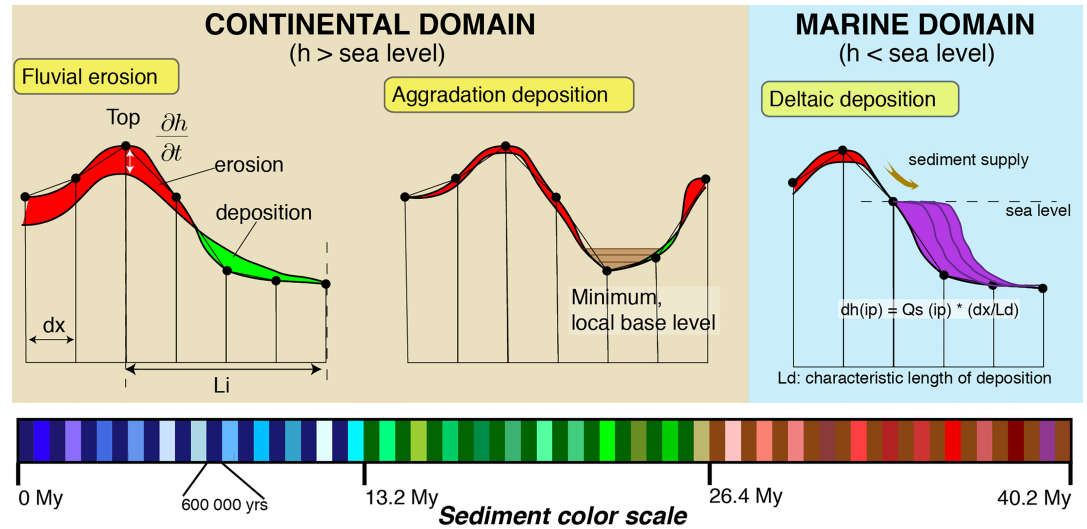
Figure 2. Surface processes model (section 2.3). Columns represent Eulerian cells. Elevation of top nodes (free surface) defines the relief, that is, topography and bathymetry. (left) 1-D implicit stream power law applied onshore. (right) Deltaic deposition using a characteristic transport length offshore.

$$\frac{\partial h}{\partial t} = -\dot{e} + \dot{d} + \dot{T}$$
$$= -\dot{e} + \dot{d}_{\text{river}} + \dot{d}_{\text{lake}} + \dot{d}_{\text{offshore}} + \dot{T}, \quad (5)$$

where h is the elevation, $\dot{e}$ is the erosion rate, $\dot{d}$ is the deposition rate, and $\dot{T}$ the tectonic uplift rate. All river profiles are first computed, and transported sediments are stored at each local minimum or at the "coast line" defined by the sea level. Sediments are then aggraded into the lakes or bypassed down to sea or outside the model domain if they reach sides when lakes are full. Sediments are finally prograded offshore below sea level.

Fluvial erosion is implemented by solving the shear-stress fluvial incision or stream power law (Howard & Kerby, 1983; Howard, 1994; Lague, 2014; Tucker & Whipple, 2002; Whipple & Tucker, 1999; Whipple, Hancock, & Anderson, 2000; Whipple et al., 2000, 1999):

$$\dot{e} = K Q_{\text{w}}{}^m s^n, \quad (6)$$

where $\dot{e}$ is the erosion rate, K is a constant called erodibility or erosion efficiency factor, Q_{w} is the stream discharge, and s the topographic slope. The stream discharge Q_{w} represents the total precipitation accumulated on the upstream part of the watershed, $Q_{\text{w}}=A \cdot P$, where P is the precipitation rate and A is upstream drainage area given by $A = \left(\frac{L_i}{1.4}\right)^{\frac{1}{0.55}}$ where L_i is the length of the drainage area or the river in our case given in kilometers (Hack, 1957; Rigon et al., 1996; Willett, 2010). A sediment transport length function $\xi(q)$ controls sediments deposition along the fluvial profile (Davy & Lague, 2009; Kooi & Beaumont, 1994; Yuan et al., 2019) where q is the stream discharge per unit of river width. The rate of fluvial deposition is controlled by

$$\dot{d}_{\text{river}} = \frac{q_{\text{s}}}{\alpha \cdot q} = \frac{q_{\text{s}}}{\xi(q)} = \frac{Q_{\text{s}}/W}{\alpha \cdot Q_{\text{w}}/W} = \frac{Q_{\text{s}}}{\alpha \cdot Q_{\text{w}}}, \quad (7)$$

where q_{s} is the sediment river load per unit of river width W, αq corresponds to the sediment transport length, where α $(s \cdot m^{-1})$ >0 allows choosing between detachment-limited (only erosion) and transport-limited (deposition is allowed) end-members. The sediment river load Q_{s} is given at each node by the amount of upstream accumulated sediments and the volume of sediments removed or deposited at this node:

$$Q_{\text{s}} = \int_L (\dot{e} - \dot{d}_{\text{river}}) \cdot W dL, \quad (8)$$

where L is the catchment length and the river width W varies as the square root of the water discharge $c \cdot \sqrt{Q_{\text{w}}}$ (Lacey, 1930; Savenije, 2003). There is a river between each local maximum and local minimum above sea level. Each river profile, given by $-\dot{e} + \dot{d}_{\text{river}}$, is computed using a 1-D implicit algorithm (Braun & Willett,

Table 2
Surface Processes Parameters

Parameter	Symbol	Units	Value
Stream power law			
Erodibility	K	$m^{1-3m} \cdot s^{m-1}$	$5 \cdot 10^{-9}$ to $5 \cdot 10^{-10}$
Precipitation	P	m/year	1.0
Area exponent	m	—	0.4
Slope exponent	n	—	1.0
River deposition			
Lacey's coefficient	c	$s^{0.5} \cdot m^{-0.5}$	3.08
Sediment coefficient	α	s/m	10^{-2}
Hillslope process			
Diffusion coefficient	D_H	m^2/year	1.0
Hack's law			
Constant factor	ka	—	1.4
Constant power	h	—	0.55
Compaction of silico-clastic sediments			
Solid grains density	ρ_g	kg/m^3	2,640
Initial porosity	ϕ^0	—	0.52
Compaction coefficient	c	m^{-1}	$4.7 \cdot 10^{-4}$

Note. Stream power law (see equation (6)), river deposition (see equations (7) and (8)), and hillslope processes and compaction (see Supporting Information S1).

2013). A constant erodibility is used for the entire model. It is assumed that the actual drainage divide in the topography is located between two nodes. The drainage divide is located between the highest node and its lowest neighbor. Consequently, if one side of the drainage divide erodes faster than the other side, the drainage divide can migrate.

In our model, deposition along the river profile only happens when the net change in elevation is positive. Most of the deposition occurs either in local minima above sea level by aggradation in lakes or when sediments are transported beneath sea level by progradation. Each local minimum above sea level is defined as a lake. The elevation of the sill defines the maximum level of sedimentation in the current lake. When a local minimum is full of sediments, then they are bypassed to the next local minimum down to the sea or leave the model domain when they reach sides. Deltaic progradation is based on a characteristic sediment transport length L_d, intended to simulate the fall out of a suspension plume (equation (9)).

$$\dot{d}_{\text{offshore}} = q_s \frac{\mathrm{d}x}{L_d}, \tag{9}$$

where q_s is the sediment discharge per unit width. To ensure mass balance, q_s at the river mouth (river that ends into the sea or into a lake above sea level) corresponds to the integrated net surface change by erosion and deposition along the river profile:

$$q_s = \int_L (\dot{e} - \dot{d}_{\text{river}})\mathrm{d}L. \tag{10}$$

All surface processes parameters are summarized in Table 2, and additional detailed explanation of the surface processes model can be found in Supporting Information S1.

3. Reference Models Without Surface Processes

We first describe the Reference Models M1 to M4 with varying crustal rheologies (R1–R4; with $f_{\text{uc}} = 30$, 1, 0.1, and 0.02) without surface processes and analyze the relief produced for these four cases (Table 3). The end-member without surface process is an important model reference that allows to separate and understand the effect of surface processes on model behavior.

3.1. Model M1, Strong Crust, f_c=30

Reference Model M1 (Figure 3a) has the strongest crustal rheology with minor decoupling in the viscous lower crust. The tectonic style of deformation is asymmetric and evolves in two phases. Phase 1

Table 3
Presented Models

Figure	Model index	Rheology	Erodibility	Sea level
Figure 3	M1	R1	No	sl1
	M2	R2	No	sl1
	M3	R3	No	sl1
	M4	R4	No	sl1
Figure 5	M5	R1	K2	sl1
	M6	R2	K2	sl1
	M7	R3	K2	sl1
	M8	R4	K2	sl1
Figure 6	M9	R1	K3	sl1
	M10	R2	K3	sl1
	M11	R3	K2–3	sl1
	M12	R4	K2–3	sl1
	M13	R1	K2	sl2
	M14	R2	K2	sl2
	M15	R3	K2	sl2
	M16	R4	K2	sl2

Note. K2 to 10^{-9}, K2–3 to $2.5.10^{-9}$, and K3 to 5.10^{-9}, and sl0 is equivalent to 0 m, sl1 to -500 m, sl2 to $-1,500$ m.

deformation is controlled by one single frictional-plastic shear zone cross cutting the strong crust and upper mantle-lithosphere, while Phase 2 is characterized by ductile necking and symmetric break up. At 5 Ma, most of the deformation is accommodated by a 45° dipping frictional-plastic shear zone that extends into the upper mantle at 55-km depth. Minor secondary localized shear zones develop in the hanging wall of the primary asymmetric normal fault zone. At 10 Ma, continued offset on the large asymmetric shear zone results in rupture of the hanging wall leading to several smaller-scale upper crustal fault blocks on top of the upper mantle-lithosphere bounded by a regional low-angle detachment. Thinning of the mantle-lithosphere and upwelling of the asthenosphere lead to Phase 2 symmetric ductile necking localizing deformation in a narrow region and lithospheric rupture at about 15 Ma. The final margin geometry is highly asymmetric with clear upper and lower plate styles originating from Phase 1. The "lower plate" margin is characterized by a single large offset normal shear zone, several upper crustal allochtonous blocks in contact with the upper mantle-lithosphere, and absent middle to lower crust (Figure 3). The "upper plate" margin in contrast is characterized by distributed small offset fault zones and a narrow tapered crustal thinning and relief gently dipping toward the distal margin.

3.2. Model M2, Intermediate Strength Crust, $f_c=1$

Model M2 has an intermediate crustal rheology with an approximate brittle layer thickness of 15 km and weak viscous middle to lower crust allowing decoupling between the strong frictional-plastic upper crust and upper mantle-lithosphere (Figures 1 and 3). This model exhibits symmetric extension during rifting resulting in narrow conjugate margin formation at ~14 Ma (Figure 3). At 5 Ma, two conjugate normal faults in the upper crust form a largely symmetric graben, while the upper mantle-lithosphere below the graben area exhibits symmetric localized deformation. Between 5 and 10 Ma, localization of deformation migrates both outward toward the proximal rift flank and inward toward the central graben. Outward migration results in symmetric horsts on both conjugate margins and minor subsidiary synthetic faults in the proximal rift flanks. At the same time, thinning of the central crustal keystone block results in a secondary symmetric graben that ruptures the upper and lower crust. Lithospheric breakup is reached at ~ 15 Ma. While some small differences can be observed in both the proximal and distal areas, the conjugate margins are largely symmetric, 110 km versus 130 km wide.

3.3. Model M3, Weak Crust, $f_c=0.1$

Model M3 has a weak crustal rheology (Figures 1 and 3). It exhibits a thin about 11-km frictional-plastic upper crust which is fully decoupled from the frictional-plastic upper mantle-lithosphere. This model
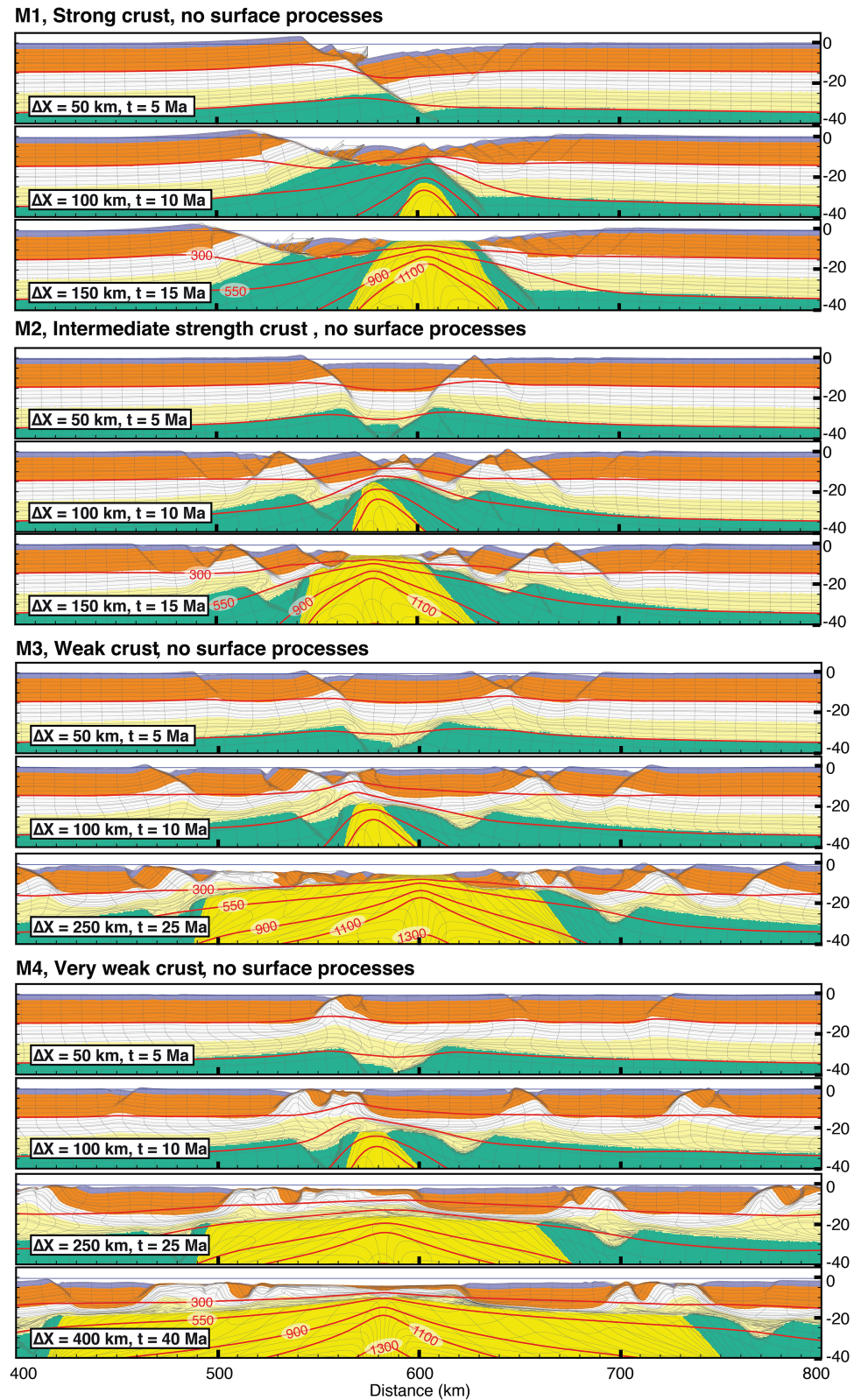
Figure 3. Time evolution of Reference Models M1 to M4 without surface processes, respectively, with strong crust rheology R1 (Wet Quartz f=30), intermediate crustal strength R2 (Wet Quartz f=1), weak crustal strength R3 (Wet Quartz f=0.1), and very weak crustal strength (Wet Quartz f=0.02). See, respectively, sections 3.1–3.4 for details and Table 3 for model details on parameters.

evolves in two phases (Figure 3). Phase 1 exhibits distributed crustal deformation decoupled from localized necking of the mantle-lithosphere. During Phase 2, crustal thinning is diachronous and localizes progressively in the distal margin resulting in wide conjugate margins with core complex formation and exhumation of middle and lower crust. Between 5 and 10 Ma, Phase 1 extension leads to widely spaced, large offset normal faults in the upper crust. Raft-like upper crustal blocks in between the normal faults exhibit very minor upper crustal extension, while the middle and lower crust at depth are moderately thinned by flow toward areas with upper crustal faulting and thinning. The mantle-lithosphere is fully ruptured at 10 Ma, while the crust is only moderately extended to a thickness of ~15–20 km. At this stage, the Moho temperature in the midcrust above the mantle necking zone increases from its initial value of 550 to ~600–700 °C. From 10 Ma onward, Phase 2 deformation localizes progressively in the distal margin, with no activity on Phase 1 proximal fault zones. Distal margin localization results in the development of a large offset low-angle detachment fault on top of the high temperature anomaly, with exhumation of middle and lower crust and formation of a core complex at 15 Ma. Continued thinning in the distal margin between 15 and 25 Ma leads to rupture of the distal margin upper crustal raft into a set of smaller fault bounded upper crustal blocks in contact with the new sublithospheric mantle. Moho temperature in the distal margin decreases to ~300 °C. The conjugate margin pair following lithospheric breakup at ~25 Ma shows a 200-km-wide margin characterized by exhumed middle and lower crust and a 160-km-wide margin with upper crustal rafts and large offset normal fault zones.

3.4. Model M4, Very Weak Crust, f_c=0.02

Model M4 has a very weak crustal rheology (Figures 1 and 3) with a frictional-plastic layer that is ~8 km thick. The very weak viscous middle and lower crust below allows for full decoupling from the upper mantle-lithosphere. M4 evolves similar to Model M3 in two phases, with Phase 1 distributed upper crustal deformation and concomitant mantle-lithosphere necking and Phase 2 progressive localization in the distal margin resulting in an ultrawide conjugate margin pair, with high-offset low-angle normal faults. The main difference with Model M3 is that Model M4 is characterized by fewer upper crustal normal faults with larger offset and more effective middle and lower crustal flow during rifting. While in M3, only one normal fault exhumes middle and lower crust, most normal faults in Model M4 accommodate significant offset leading to "core complex" style deformation on each of these. Phase 1 extension until about 20 Ma involves distributed crustal extension with four main upper crustal faults that fully rupture the upper crust and exhume midcrust to the surface, while at the same time, localized deformation at depth ruptures the lithospheric mantle. Upper crustal thinning is balanced by middle and lower crust flowing into the necking areas. Crustal raft zones in between the necking zones exhibit very limited upper crustal extension, whereas viscous flow of the middle and lower crust results in crustal thinning and sag-type subsidence (Figure 3). Similar to Model M3, mantle-lithospheric necking and thermal advection result in a transient increase of the Moho temperature to ~600–700 °C in the central part of the rift around 10 Ma. Phase 2 extension from ~20 Ma exhibits progressive localization of crustal thinning in the distal margin. Most deformation during this stage is accommodated by increased offset on the most distal low-angle normal fault. However, in contrast to Model M3, proximal normal faults remain active throughout the rift history. Lithospheric breakup occurs at ~40–45 Ma resulting in about 280-km-wide conjugate margins. The structure of the distal margins is significantly different, with one showing low-angle detachments and exhumed midcrust and the other formed by a wide upper crustal raft zone.

3.5. Topography Characteristics for Models M1–M4

Models M1–M4 result in highly contrasting topographies. Based on topographic characteristics at 20 Ma, three groups can be distinguished (Figure 4). (1) Strong crustal rheologies as exemplified by Model M1 are characterized by asymmetric high rift flanks with a maximum elevation of 2,500 m, a narrow deep basin with relatively smooth relief resulting from few normal faults. (2) Intermediate strength rheologies as in Model M2 are characterized by low rift flank topography with a maximum elevation of 1,000 m and significant relief inside the basin resulting from multiple normal faults and rotated hanging wall crest. (3) Weak to very weak crustal rheologies as in Models M3 and M4 are characterized by absent rift flank topography, very wide margins, and significant relief offshore resulting from multiple fault blocks and large offset low-angle detachment faults with footwall-exhumation of middle and lower crust forming core complex structures on the sea-floor within the continental crust.
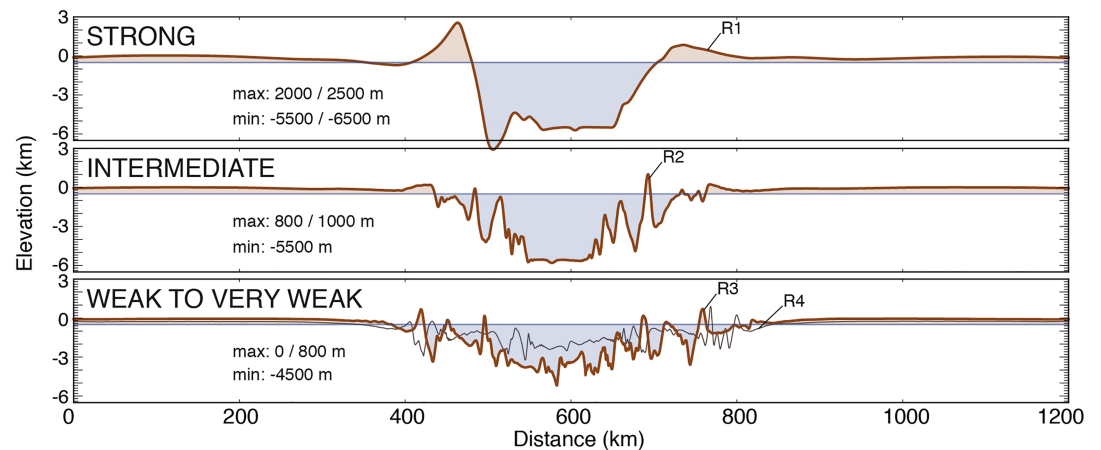
Figure 4. Topography for Models M1 to M4 without surface processes. (1) Strong crust coupled to mantle with asymmetric high rift flanks, (2) intermediate crustal strength with low rift flank topography and significant relief inside the basin resulting from multiple normal faults and rotated hanging wall crest, and (3) weak to very weak crustal rheologies with absent rift flank topography, very wide margins, and significant relief offshore resulting from multiple fault blocks and large offset low-angle detachment faults. See presented models on Table 3.

4. Reference Models With Surface Processes

A relatively limited range of erodibility (1 order of magnitude in our model; see Tables 2 and 3) results in end-member behavior with either limited or highly efficient (close to complete) erosion. We next present Rift Models M5–M8 with Rheologies R1–R4 including surface processes with intermediate fluvial erosion efficiency ($K = K2 = 1 \times 10^{-9}\ \mathrm{m}^{1-3m}\ \mathrm{s}^{m-1}$) and high sea level fixed at -500 m below the initial reference topography at $z=0$ m (Table 3).

4.1. Model M5, Strong Crust, f_c=30, Intermediate Erodibility, High Sea Level

Model M5 (Figures 1 and 5) can be compared with Model M1 that has the same rheology but no surface processes. Early in its evolution until about 10 Ma, this model erodes the rift flanks that provide the limits to a narrow drainage basin. Sediment accumulation on the hanging wall of the large asymmetric normal fault results in longer activity and increased offset of this major basin bounding fault in comparison to Model M1. At 10 Ma, thinning of the mantle-lithosphere at depth and thermal upwelling occur coeval with necking of the upper crustal hanging wall block resulting in a major listric normal fault antithetic to the initial asymmetric fault zone. Erosion of the divide and drainage capture on the (right) upper plate margin around 10 Ma results in significantly increased sediment export into the basin and deposition of a secondary sediment wedge on top of a listric normal fault zone bordering new asthenospheric mantle. The (left) "lower plate" margin exhibits drainage capture around 15 Ma with associated increased sediment supply to the basin. Continued erosion of the large drainage basin and sediment transport results in a narrow overfilled lower plate basin following lithosphere breakup. Localized deformation and thermal upwelling in the distal rift zone ruptures the secondary sediment wedge with part of it ending up in the distal part of the lower plate margin. The resulting conjugate margins are highly asymmetric both in terms of structure and sediment distribution. The (left) lower plate margin accumulates most of the sediments and exhibits large displacement on a single normal fault, instead of multiple small fault bounded blocks in Model M1. The (right) "upper plate" margin exhibits few faults with little offset and preserves early postrift prograding sediments.

4.2. Model M6, Intermediate Strength Crust, f_c=1, Intermediate Erodibility, High Sea Level

Model M6 has a similar evolution as M2, however, with a number of notable differences (Figure 5). During a first phase, M6 similar to M2 initializes deformation in a symmetric graben with two main border faults. However, in contrast to M2, M6 does not show any outward migration of faulting and strain continues to accumulate on the primary border faults during Phase 2. Continued proximal deposition results in
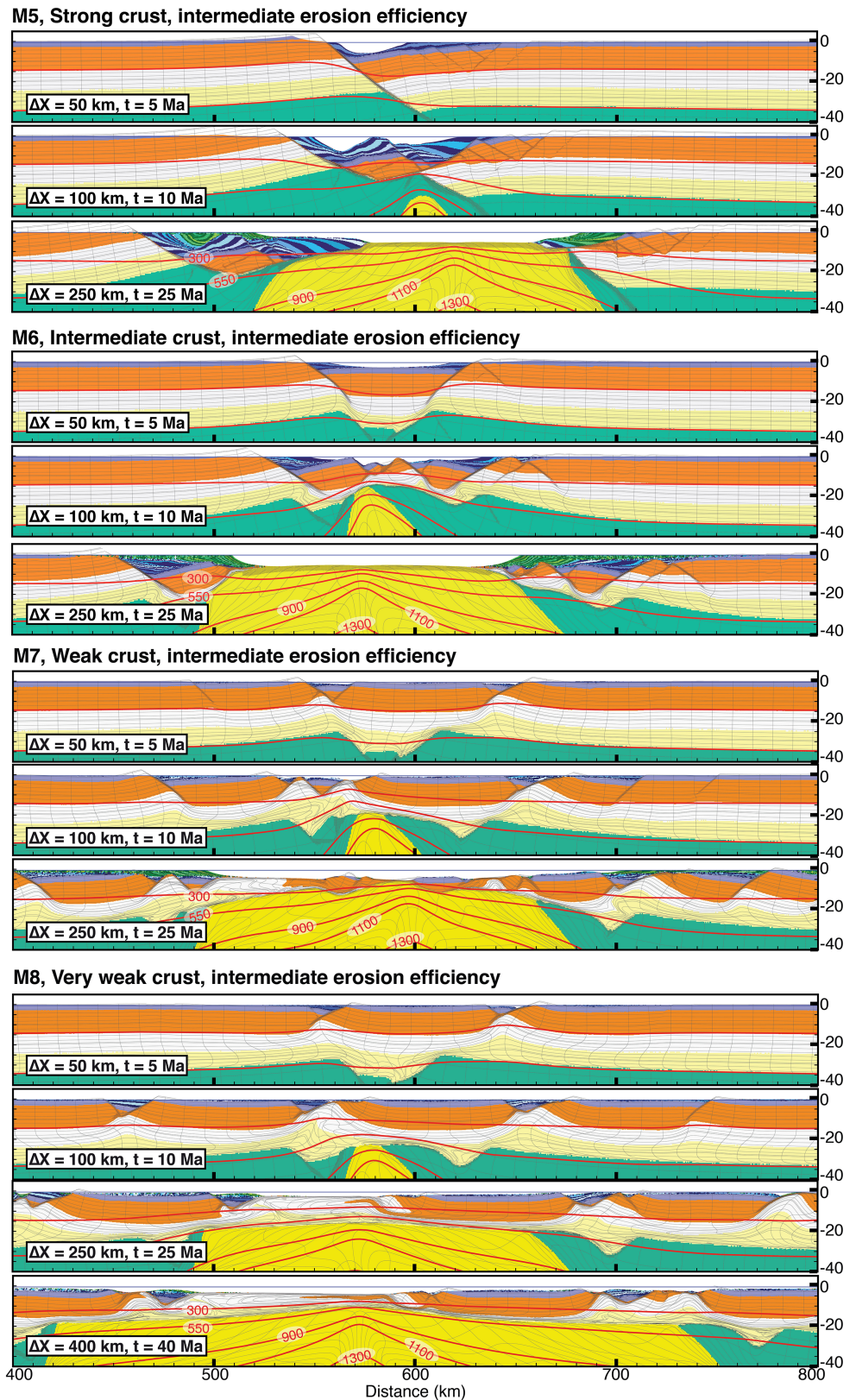
Figure 5. Time evolution of Models M5 to M8 with surface processes (intermediate erosion efficiency *K*2, see Tables 2 and 3) for Rheologies R1 (Wet Quartz *f*=30), R2 (Wet Quartz *f*=1), R3 (Wet Quartz *f*=0.1), and R4 (Wet Quartz *f*=0.02). The sea level "*sl1*" is fixed at −500 m. See sections 4.1–4.4 for detailed description and Tables 2 and 3 for model parameters.

significantly larger offset and fewer crustal fault bounded blocks. Upon lithospheric breakup around 14 Ma, continued sediment supply results in filling the proximal margin and progradation to the distal margin. As a result of enhanced offset on fewer normal fault zones, the conjugate margins are significantly narrower than in Model M2.

4.3. Model M7, Weak Crust, f_c=0.1, Intermediate Erodibility, High Sea Level

Model M7 with a weak crust can be compared with the equivalent M3 without surface processes (Figures 1 and 5). Models with weak crust result in very moderate to absent rift flank topography (Figure 4). Given a relatively high sea level, these models have limited potential to produce sediment discharge to the extending margin, which explains the sediment starved character of Model M7. Model M7 exhibits, similar to M3, two characteristic phases of deformation with Phase 1 distributed crustal extension concomitant with narrow mantle-lithospheric necking and Phase 2 progress localization of crustal thinning in the distal margin. Notable differences during Phase 1 up to ~15 Ma include fewer normal fault zones accommodating asymmetric upper crustal extension and synthetic basinward dipping normal faults with footwall erosion and hanging wall deposition. During Phase 2, onward from ~15 Ma, strain localization migrates to the distal margin leading to large offset low-angle normal faults and isolated upper crustal fault bounded blocks in the distal margin in contact with new asthenospheric mantle. However, proximal synthetic faults zones remain active and continue to accumulate limited sediment volumes exported from the onshore drainage basin.

4.4. Model M8, Very Weak Crust, f_c=0.02, Intermediate Erodibility, High Sea Level

As in Model M7, absent rift flank topography limits the amount of sediment that can be produced with relatively high sea level. Model M8 with very weak crust shows, however, some notable differences in comparison with the equivalent Model M4 without surface processes (Figure 5). During Phase 1 up to 10 Ma, extension is accommodated on four upper crustal grabens with large offset low-angle normal faults forming asymmetric basins. Local footwall topography is efficiently removed by erosion resulting in additional local sediment supply to these small graben systems. Lithosphere rupture results in increased Moho temperature in the central part of the model. During Phase 2 from ~15 Ma, deformation localizes progressively in the distal margin, with large offset low-angle normal faults accommodating most of the extension, however, with continued offset in proximal grabens. Middle and lower crustal flow to the necking areas results in "sag"-type subsidence of the intermediate upper crustal rafts. Late syn-rift sediments are absent because the entire model domain is below sea level. Crustal thickness at breakup around 40 Ma is ~33 km in the onshore area resulting in topography at approximately −250 m below sea level explaining the absence of late syn-rift sediments.

4.5. Model Sensitivity to High Erodibility

Models M9 to M12 explore sensitivity to increased erodibility for systems with strong to very weak crustal rheology and high sea level (Figure 6a). For each model, the geometry is shown close to lithosphere breakup (see Movies S1–S16 for model animation). All models show significantly higher sediment input into the basin area throughout their evolution. For the strong crust Case M9, rift flank topography is efficiently eroded with high early sediment export into the basin resulting in a crustal-scale asymmetric half graben. Most of the strain localizes on a single border fault, and minor conjugate shear zones accommodate hanging wall deformation. Following lithospheric breakup, continued sediment discharge onto the margin creates thick growth fault bordering prograding wedges on the asymmetric conjugate margins. The intermediate strength crust Model M10 shows a similar evolution while evolving in a symmetric rift style. Efficient erosion of the rift flanks on both sides results in high sediment discharge and enhanced offset of the symmetric graben early in its evolution. During and following breakup, continued deposition leads to normal fault bounded growth sequences on new "oceanic" sublithospheric mantle, in this case resulting in more symmetric conjugate margins. Weak crust Model M11 evolves similarly to Model M6 that was characterized by a lower erodibility. A first stage of early distributed crustal extension is followed by progressive necking in the distal margin. Low rift flank topography limits early sediment export to the basin. During its later stage, the large onshore drainage area provides significant higher sediment input into the distal basin area. Late stage prograding sediments bypass early syn-rift deposit and enhance a distal margin crustal-scale shear zone rooting in the midcrust, thus providing significant accommodation space. For very weak crust Model M12, the increased erosion rates result in early sediment input to the distal margin. Deposition in the
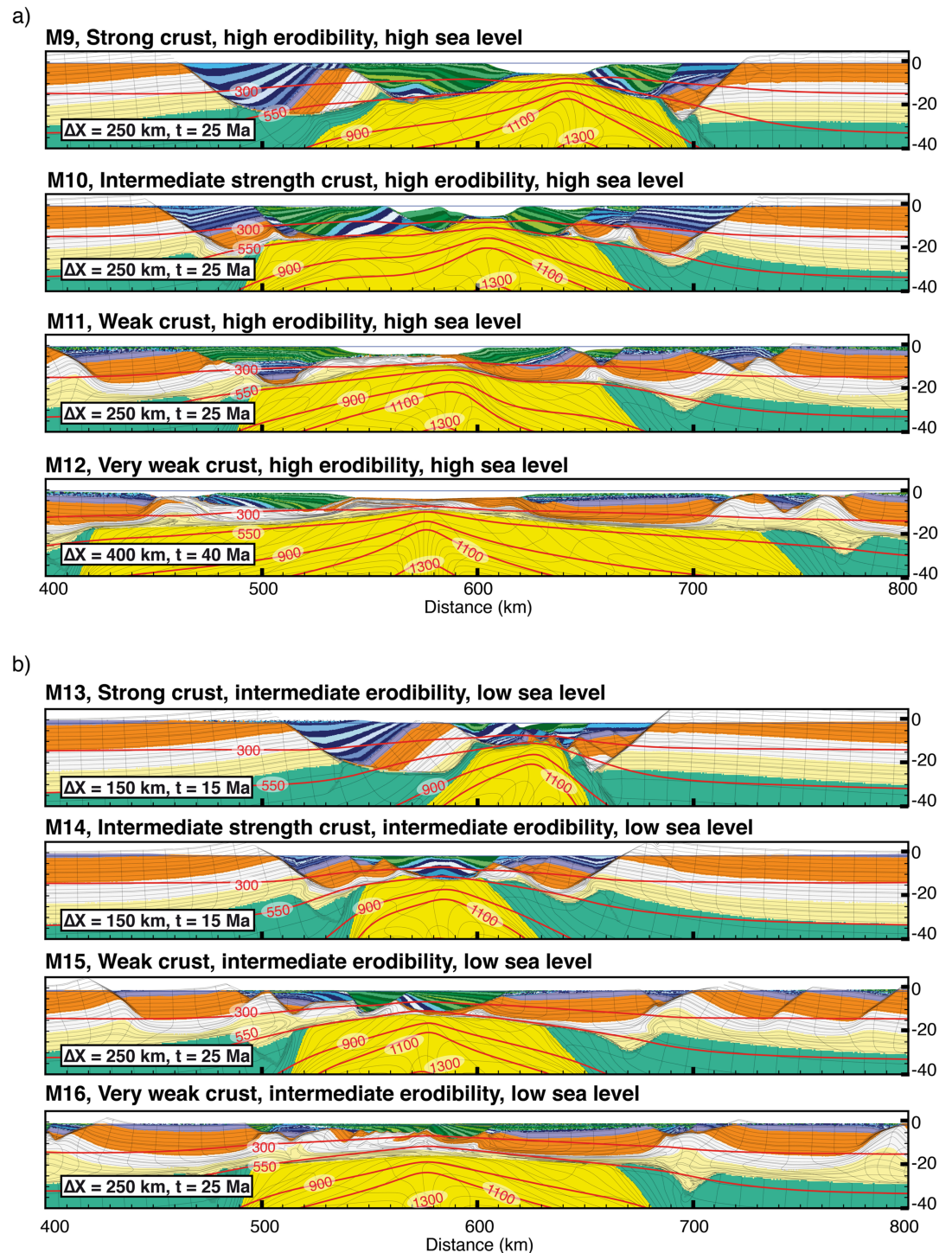
Figure 6. Final architecture for models with surface processes considering (a) high erosion efficiency $K3$ and a sea level "*sl1*" at −500 m (Models M9–M12 with Rheologies R1–R4; Table 3) and (b) low sea level "*sl2*" fixed at −1,500 m and an intermediate erosion efficiency $K2$ (Models M13–M16 with Rheologies R1–R4; see Table 3). See sections 4.5 and 4.6 for detailed description and Tables 2 and 3 for model parameters.

distal margin interacts with the formation of a large offset low-angle normal fault exhuming midcrust at the base of the sediments. Late in its rift evolution progressive thinning of the distal margin over a wide area results in necking of this sedimentary wedge and formation of a late stage core complex. The distal margin

exhibits also broad platform-type deposition on crustal rafts with very minor upper crustal extension and subsidence resulting from middle and lower crustal removal similar to Model M7.

4.6. Model Sensitivity to Low Sea Level

Models M13 to M16 test sensitivity to low sea level at −1,500 m (Figure 6b), with the reference intermediate erodibility and varying crustal rheology (Table 3). Lowering sea level has two main effects. (1) It increases the amount of onshore upper crust that can potentially be eroded and produce sediment export to the rifted margin. (2) It reduces at the same time the accommodation space available in the rifted conjugate margin resulting in lower sediment thicknesses in the proximal basin areas and promoting sediment bypass to the distal margin. Increased sediment export can be observed in all four models with low sea level. Compared to Models M5 and M6 with strong and intermediate strength crust, Models M13 and M14 show significantly greater deposition and associated erosion of the rift flanks at 15 Ma resulting in increased fault offset on the primary basin bounding normal fault zones. Weak and very weak crust Models M15 and M16 exhibit predominant bypass and erosion of proximal rift basins and deposition in the distal margin illustrating effect (2). Interaction between deposition and large offset low-angle normal fault zones in these models leads to large tilted sedimentary basins in the distal margin.

5. Discussion

We first interpret the first-order factors controlling the structural style of rift and passive margin formation in the models. We then identify and discuss the feedback relations between surface processes and tectonics. Model predictions are compared with observations from natural systems, and finally, limitations of the modeling approach are discussed.

5.1. Factors Controlling the Structural Style of Passive Margin Formation

Lithospheric rheological stratification provides the main control on the structural style of rift and passive margin formation. The structural style of passive margins is characterized by the nature and distribution of normal faulting and by its morphology (margin width, onshore topography, and top basement geometry offshore). Models characterized by limited to absent decoupling between the strong frictional-plastic crust and upper mantle layers promote narrow rifts, with most extension accommodated on few large offset listric normal faults, similar to Type 1A margins as described by Huismans and Beaumont (2011, 2014) and Buck (1991). In contrast, weak crust cases with efficient decoupling between a thin frictional-plastic upper crustal layer and the strong mantle-lithosphere below result in highly depth-dependent extension with crustal extension distributed over a wide area and concomitant narrow rupturing of the lower lithosphere, as in Type 2 margins (e.g., Huismans & Beaumont, 2011, 2014; Svartman Dias et al., 2015).

Narrow Type 1 margins as represented by Models 1 and 2 and variations with surface processes are characterized by high angle normal faults and a high crustal strength that allows for high and narrow rift flank topography onshore. In contrast, wide Type 2 margins as in Models 3 and 4, the weak middle and lower crust allows for (1) distributed crustal deformation and fault migration, (2) low or absent rift flank topography, (3) large offset normal faults with hanging wall and footwall rotation and exhumation of midcrust to the surface following the rolling-hinge model (e.g., Lavier et al., 1999), (4) middle and lower crustal flows toward the distal margin, and (5) formation of crustal raft with midlower crust removal and limited upper crustal extension resulting in sag-type subsidence.

5.2. Interaction and Feedback Between Surface Processes and Rifted Margin Formation

The forward models presented here allow to identify the following four feedback relations between surface processes and tectonic deformation during rifted margin formation (Figure 7). (1) Footwall unloading by erosion and hanging wall loading by deposition promote strain localization and enhance large offset asymmetric normal fault growth (Figure 7a) where the offset is mainly controlled by hanging wall subsidence and footwall erosion has a more reduced effect on fault displacement. (2) Progressive infill (and footwall erosion) from proximal to more distal half grabens promotes the formation of synthetic sets of basinward dipping normal faults. This interaction is predominantly inferred for intermediate crustal strength cases (Figure 7b). (3) Sediment loading on top of undeformed crustal rafts in Type 2 cases enhances middle and lower crustal flow resulting in sag basin subsidence (Figure 7c). (4) High sediment supply to the distal margin in very weak
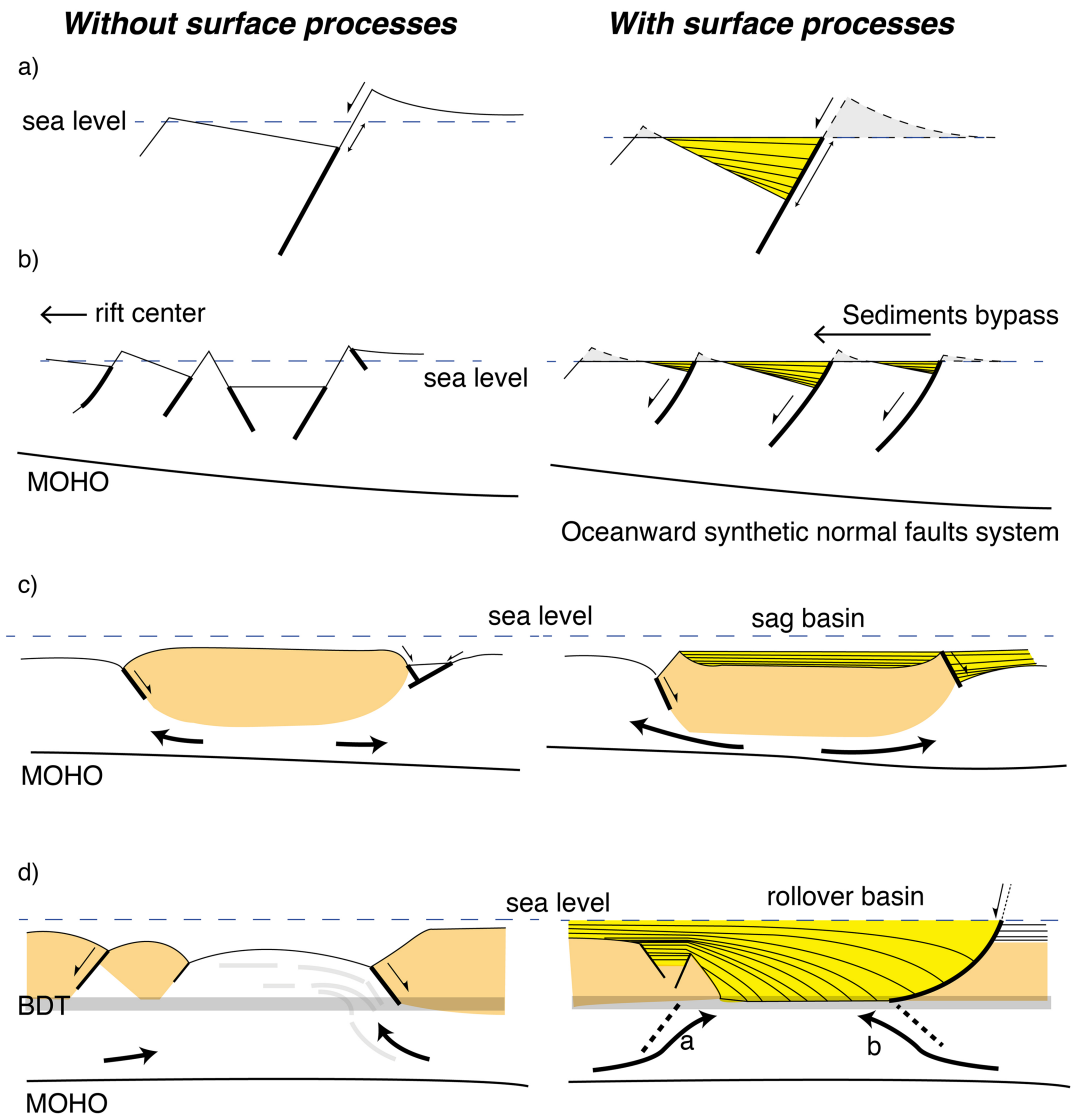
Without surface processes   **With surface processes**

Figure 7. Feedback between tectonics and surface processes during rifting. (a) Erosion and deposition promote strain localization and enhance large offset asymmetric normal fault growth. (b) Progressive infill from proximal to more distal half grabens promotes the formation of synthetic sets of basinward dipping normal faults for intermediate crustal strength cases. (c) Sediment loading on top of undeformed crustal rafts in weak crust cases enhances middle and lower crustal flow resulting in sag basin subsidence. (d) Interaction of high sediment supply to the distal margin in very weak crust cases results in detachment-based rollover sedimentary basins. The two arrows (a) and (b) represent the two observed types of midlower crustal flow beneath such extensional system.

crust Type 2 systems results in detachment-based rollover sedimentary basins, where extension is accommodated by listric faults that root at depth in a flat detachment (Figure 7d).

These feedbacks have consequences for fault offset, margin width, and time of crustal breakup (Figures 8 and 9). The structural evolution cannot be easily compared between the models as the initial structural inheritance and the nonlinearity of each numerical simulation with different conditions of surface processes introduce variations to timing of initiation and abandonment of individual faults. However, for models with a strong crust, the proximal normal fault is a systematic feature that we use to compare fault offset with changing erodibility. The proximal normal fault in Model 1 without surface processes exhibits 32 km of offset (Figures 8). With increasing surface process, efficiency fault offset increases progressively to 65 km for complete footwall erosion and hanging wall deposition (Figure 8). To first order proximal and distal margins
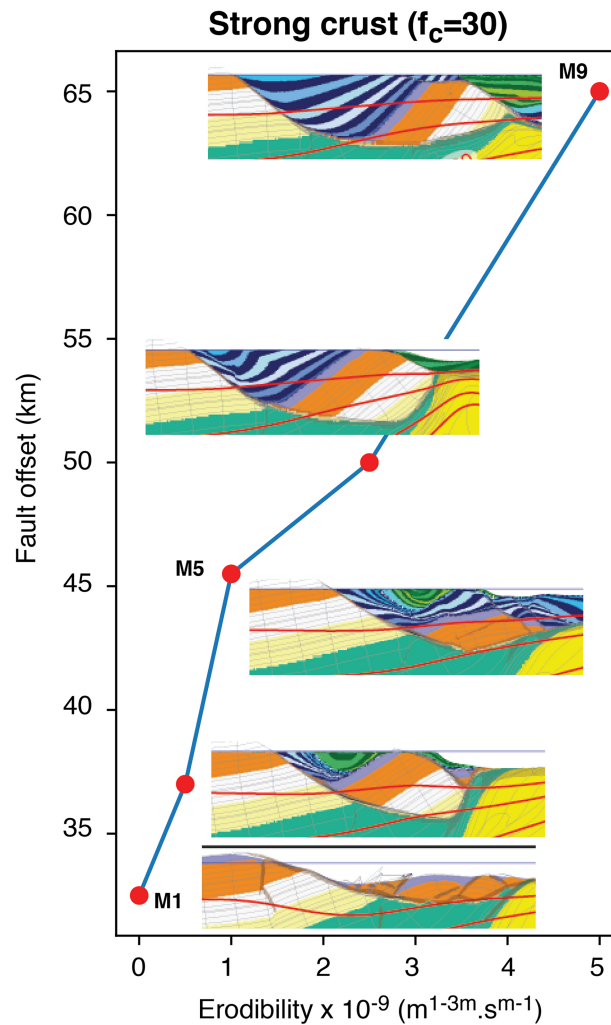
Figure 8. Fault offset measured along the proximal normal fault in experiments with strong crust rheology (R1).

width is controlled by crustal rheology (Figure 9a). Surface processes provide opposite effects on margin width for strong versus weak rheologies. When the crust is strong (R1) or has an intermediate strength (R2), proximal margin width decreases with erodibility owing to efficient strain localization, whereas distal margin width increases with increasing erodibility resulting from efficient hanging wall block rotation along a detachment fault coupled to exhumed mantle. In contrast, when the crust is weak (Rheologies R3 and R4), lower crustal flow toward the rift center due to mass redistribution by surface processes allows for wider proximal and distal margin widths with increasing sediment input. The timing of crustal breakup is relatively insensitive to erodibility for strong and intermediate crustal rheologies (R1 and R2), whereas for weak crustal rheology (R3), the time of crustal breakup increases linearly with increasing erodibility (Figure 9b).

These feedbacks also have consequences for onshore erosion and topography and for offshore sediment supply and stratigraphy. The evolution of the topography onshore controls sediment supply through time. High sediment supply during rifting is enhanced by high onshore paleotopography, large source drainage area, and high erosion rate. In our models, rift-related topography is relatively quickly eroded (Figure 10). Long-term sustained sediment supply to the rift basins requires elevated onshore drainage basins. Rift flank erosion leads to migration and retreat of the drainage divide and the formation of a rift escarpment. Drainage capture triggers a transient phase of fluvial nick point migration followed by formation of a new drainage
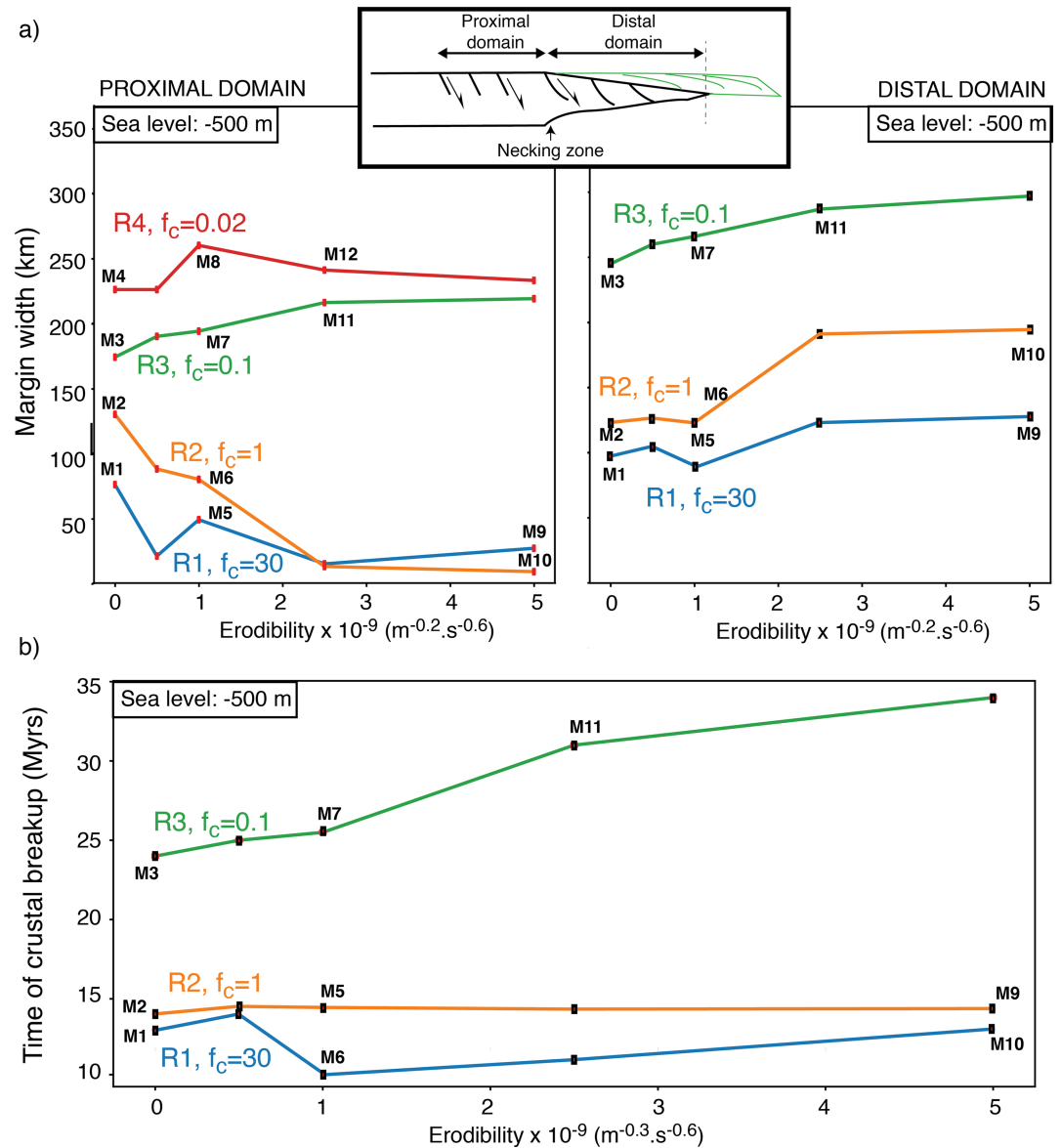
Figure 9. Comparison of margin width (a) and time of crustal breakup (b) for different values of erodibility. The proximal margin width is defined after crustal breakup as the distance between the first proximal normal fault and the necking zone (see small inset on top). Margin widths include both conjugate margins. The very weak crust case is not represented for distal margin width measurements and for time of crustal breakup since these models do not reach crustal breakup at 40 Myr of extension.

divide resulting from regional isostatic uplift. Finally, we distinguish three characteristic stratigraphic architectures:

1. Fault-bounded symmetric or asymmetric basins with growth strata (Figures 7a and 7b),
2. Sag basin deposition on top of crustal rafts with midlower crustal thinning (Figure 7c), and
3. Rollover sedimentary basins with large sections of tilted deposits on top of a flat horizontal detachment fault (Figure 7d).

5.3. Comparison With Earlier Studies

The variation of rift width with changing crustal rheology is well established and documented by a range of modeling studies (e.g., Huismans & Beaumont, 2002, 2003, 2008, 2011, 2014; Brune et al., 2014; Svartman Dias et al., 2015; Tetreault & Buiter, 2018). In contrast to Brune et al. (2014) and Andrés-Martínez et al.
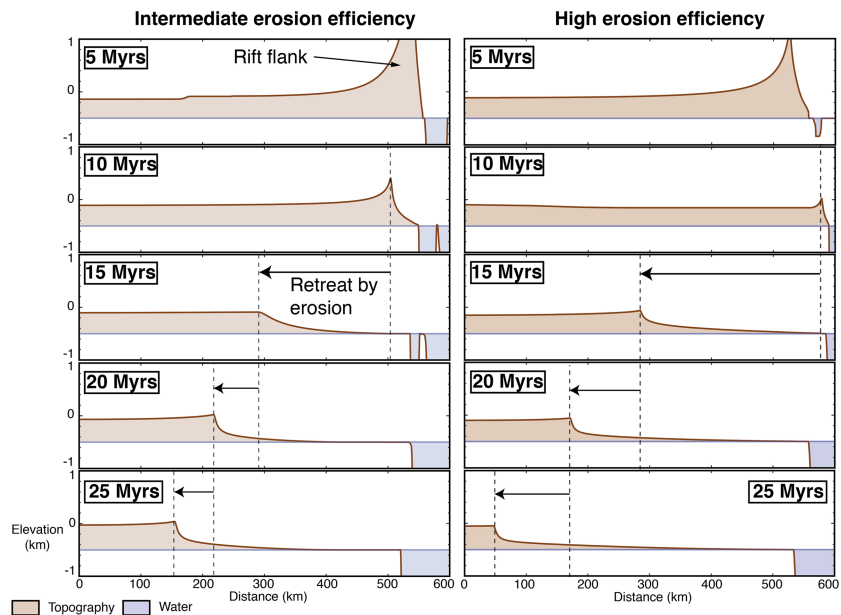
Figure 10. Characteristic topography evolution with time (left half of the model, 0–600 km) for intermediate and high erodibility, respectively, Models M5 and M9 (Table 3). Flank retreat accelerates with the drainage capture of the hinterland of the rift flank (between 10 and 15 Myr for intermediate erodibility) and slows down after formation of a new drainage divide resulting from the isostatic response to erosion onshore (i.e., at 15 Myr with intermediate erodibility). This behavior is accelerated with high erosion efficiency.

(2019), our models exhibit symmetric margins and lack lateral rift migration and large-scale margin asymmetry. The strong localization in these studies results from the combined effects of frictional-plastic strain weakening (included in our models) and viscous strain weakening (not included in our models) that cause the asymmetry (lateral rift migration) as also shown by Huismans and Beaumont (2003).

Several earlier modeling studies explored the interaction and feedback between rifting and surface processes. The feedback of footwall erosion and hanging wall deposition in enhancing fault offset in half grabens described hereby was similarly identified by Olive et al. (2014) and Andrés-Martínez et al. (2019) and suggested by Maniatis et al. (2009). As also shown by these studies, the reduction of the topographic load and flexural force through footwall erosion increase fault life span. The effect of erosion on fault offset is especially effective in the proximal domain of rifted margins where normal faults result in topography above sea level. There appears to be an optimal range of brittle layer thickness (10–20 km) where the feedback of erosion is most pronounced in our models. Lower brittle layer thickness leads to large offset no matter the erosion efficiency, whereas greater brittle layer thickness leads to reduced sensitivity to footwall erosion as also shown by Olive et al. (2014). In the distal margin for strong crust cases with a thick upper crustal brittle layer, normal fault offset is mainly controlled by hanging wall block rotation, and deposition may enhance fault offset.

In contrast to Burov and Poliakov (2001, 2003), we do not observe outward midlower crustal flow toward the rift flanks and related stabilization of rift shoulder uplift with high sedimentation rate. Midlower crustal flow in our models occurs generally in the direction of a negative pressure gradient, that is from the elevated rift margins to the subsiding basin center, provided that the crust is sufficiently weak. With weak crustal rheologies, high sedimentation rate enhances midlower crustal flow toward the rift center leading to wide margins and delaying distal margin subsidence.

In contrast with Bialas and Buck (2009), we observe that distal margin width increases with high sediment deposition whatever the crustal rheology. The time of crustal breakup is relatively insensitive to sediment deposition for strong and intermediate crustal rheologies and increases linearly for cases with a weak crust. Only the proximal domains of cases with strong and intermediate crustal rheology are narrower with efficient surface processes. The effect of surface processes on fault migration and interaction is important, e.g. feedback 2, as demonstrated by the highly different fault evolution with varying surface processes
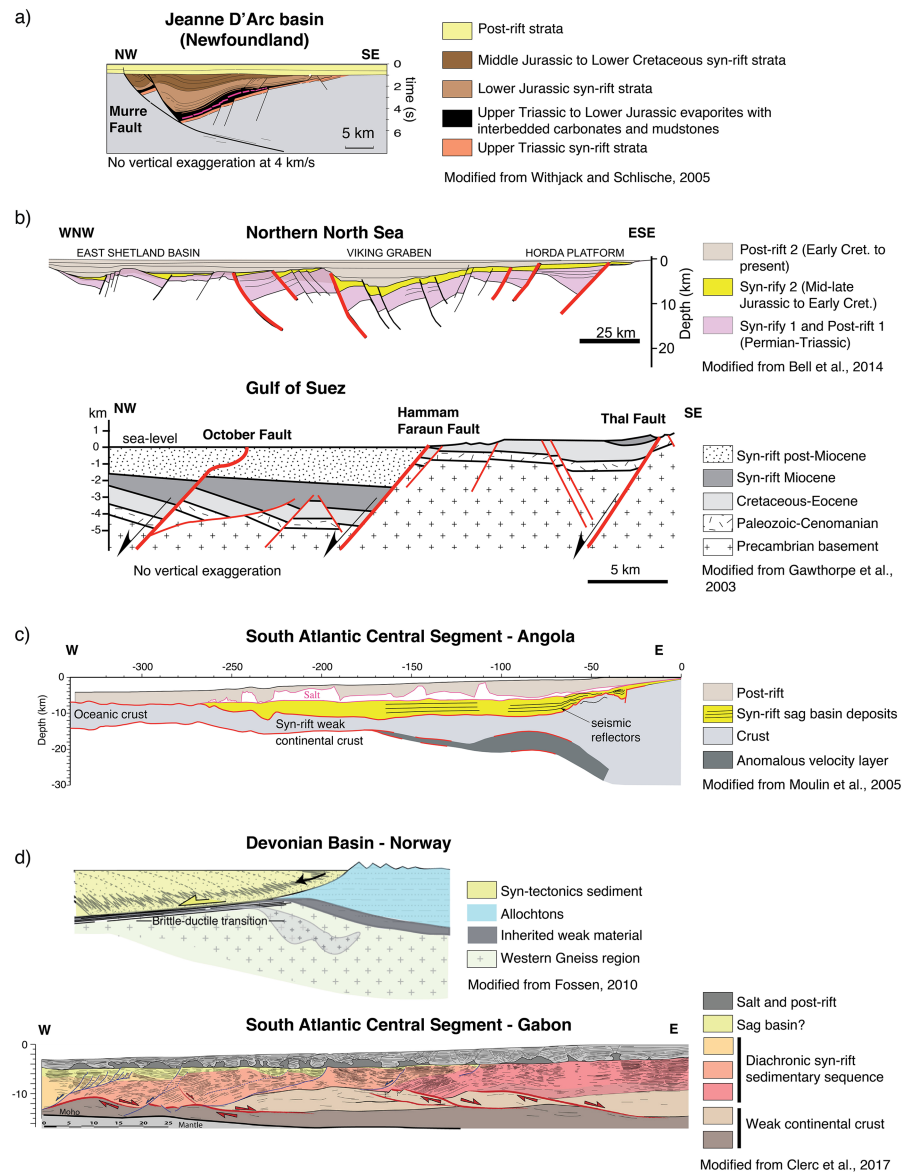
Figure 11. Natural cases that provide examples of the inferred feedback relations between surface processes and tectonics during extensional basins formation. (a) Enhanced normal fault offset with high syn-rift sediment supply. Example from Jeanne d'Arc Basin on the Newfoundland margin (Schlische, 2003; Withjack et al., 1998; Withjack & Schlische, 2005). (b) Enhanced synthetic basinward normal faults by syn-rift deposition. Examples from the Northern North Sea (Bell et al., 2014; Cowie et al., 2005) and the Gulf of Suez (Gawthorpe et al., 2003). (c) Middle and lower crustal thinning. Example from sag basin deposition along the central South Atlantic margin (Karner et al., 2003; Moulin et al., 2005). (d) Tilted sedimentary sections on top of a low-angle detachment. Examples from Devonian basins onshore Norway (e.g., Fossen, 2010; Fossen et al., 2016; Seranne & Seguret, 1987) and in the distal part of the wide Gabon margin (Clerc et al., 2017).

efficiency. This is consistent with feedback relations inferred by previous modeling studies (Olive et al., 2014; Buiter et al., 2008; Choi et al., 2013).

5.4. Natural Cases

We next discuss briefly some natural cases that may provide examples of the inferred four feedback relations between surface processes and tectonics during extensional basins formation. (1) High offset overfilled half grabens such as the Jeanne d'Arc Basin on the Newfoundland margin (Schlische, 2003; Withjack et al., 1998; Withjack & Schlische, 2005) may provide an example of enhanced normal fault offset with high syn-rift

sediment supply (Figure 11a). (2) Many rifts and passive margins as for example the Northern North Sea (Bell et al., 2014; Cowie et al., 2005) and the Gulf of Suez (Gawthorpe et al., 2003) exhibit sets of synthetic basinward normal faults (Figure 11b). We suggest, based on the understanding of the feedback relations developed here, that synthetic basinward faulting may be enhanced by syn-rift deposition. (3) Sag deposition along the central South Atlantic margin on top of undeformed basement has been explained as resulting from middle and lower crustal thinning (Karner et al., 2003; Moulin et al., 2005; Figure 11c). Middle to lower crustal flow in wide Type 2 margins as identified here may explain the inferred crustal thinning. (4) Tilted sedimentary sections on top of a low-angle detachment as observed in Devonian basins onshore Norway (e.g., Fossen et al., 2016; Seranne & Seguret, 1987) and in the distal part of the wide Gabon margin (Clerc et al., 2017; Figure 11d) are consistent with rollover basins as predicted here in case of high sediment supply in weak Type 2 extensional systems.

5.5. Model Limitations

Our modeling approach is inherently 2-D and does not take into account any 3-D variation of tectonic deformation and landscape response. Drainage divide migration (Goren et al., 2014; Braun, 2018) and average topography by river incision (Willett, 2010) could also be modeled with analytical solutions. However, sensitivity tests using a 2-D tectonic model coupled to a 2-D plan form surface process model indicate very similar behavior (Beucher & Huismans, 2016). The model uses a viscoplastic rheology and does not include elasticity. The viscoplastic behavior does, however, exhibit regional and local flexural uplift in response to tectonic and crustal loading, and the model is therefore appropriate for exploring the long-term interactions between surface processes and tectonics. However, the flexural wavelength in our model is rate dependent, while it is rate independent with elasticity. The effect of loading and unloading may therefore generate some differences in term of flexural response and influence fault offset and patterns of fault migration (Olive et al., 2016).

The surface process model does not include short-term variations in precipitation, the effect of storms, and orographic effects, while potentially important are beyond the scope of the present study. Other effects such as sediment blanketing that may affect the thermal structure during rifting and will potentially influence tectonic deformation are not included here and deserve further study.

6. Conclusion

We use state of the art 2-D forward dynamic models to understand the interaction and feedback between tectonics and surface processes during lithosphere extension and rifted margin formation. The arbitrary Langrangian Eulerian high-resolution 2-D model solves for viscoplastic deformation coupled to a mass balancing fluvial erosion-submarine delta deposition model that allows to bridge a large range of scales from lithosphere-upper mantle scale to the scale of the sedimentary basin. We evaluate competing controls on the structural style of rifted margin formation, associated onshore tectonic morphology, and offshore sedimentary basin architecture and test the sensitivity to crustal strength, fluvial erosion efficiency, and "sea level." Based on our forward models, we conclude the following:

1. The primary control on the structural style of rift and passive margin formation is provided by crustal rheology which is consistent with earlier studies. Type 1 narrow continental margins with strong crust and high coupling with mantle-lithosphere exhibit few large offset listric faults that branch into the mantle. Type 2 wide continental margins with weak crust and high decoupling between upper crust and mantle-lithosphere exhibit distributed deformation and few large offset detachment faults.
2. Footwall unloading by erosion and hanging wall loading by deposition provide a first-order feedback on tectonic deformation by enhancing asymmetric normal fault growth and prolonging fault activity.
3. For intermediate crustal strength, footwall unloading by erosion and hanging wall loading by deposition together with sediment bypass promote the formation of sets of basinward dipping synthetic faults in the proximal margin.
4. Sediment loading on top of undeformed crustal rafts in weak Type 2 margins enhances middle and lower crustal flow resulting in sag basin subsidence.
5. High sediment supply to the distal margin in very weak crust Type 2 systems results in detachment-based rollover sedimentary basins.
6. Erosion efficiency and drainage area provide the first-order control on sediment supply during rifting.

7. Rift-related topography is relatively quickly eroded.
8. Long-term sustained sediment supply to the rift basins requires elevated onshore drainage basins.

References

Albertz, M., & Ings, S. J. (2012). Some consequences of mechanical stratification in basin-scale numerical models of passive-margin salt tectonics. *Geological Society, London, Special Publications*, *363*(1), 303–330. https://doi.org/10.1144/SP363.14

Andrés-Martínez, M., Pérez-Gussinyé, M., Armitage, J., & Morgan, J. P. (2019). Thermomechanical implications of sediment transport for the architecture and evolution of continental rifts and margins. *Tectonics*, *38*, 641–665. https://doi.org/10.1029/2018TC005346

Athy, L. F. (1930). Density, porosity, and compaction of sedimentary rocks. *AAPG Bulletin*, *14*, 1–24. https://doi.org/10.1306/3D93289E-16B1-11D7-864500010

Avouac, J. P., & Burov, E. (1996). Erosion as a driving mechanism of intracontinental mountain growth. *Journal of Geophysical Research*, *101*(B8), 17,747–17,769. https://doi.org/10.1029/96JB01344

Beaumont, C., Fullsack, P., & Hamilton, J. (1992). Erosional control of active compressional orogens. In McClay, K. R. (Ed.), *Thrust tectonics*. Dordrecht: Springer Netherlands, pp. 1–18. https://doi.org/10.1007/978-94-011-3066-0_1

Beaumont, C., Jamieson, R. A., Nguyen, M. H., & Lee, B. (2001). Himalayan tectonics explained by extrusion of a low-viscosity crustal channel coupled to focused surface denudation. *Nature*, *414*(6865), 738–742. https://doi.org/10.1038/414738a

Bell, R. E., Jackson, C. A.-L., Whipp, P. S., & Clements, B. (2014). Strain migration during multiphase extension: Observations from the northern north sea. *Tectonics*, *33*, 1936–1963. https://doi.org/10.1002/2014TC003551

Beucher, R., & Huismans, R. S. (2016). Morphotectonic evolution of passive margins undergoing active surface processes: Large-scale experiments using numerical models. In *EGU General Assembly Conference Abstracts*, *18*, id. EPSC2016–6575, paper presented at EGU General Assembly held 17–22 April, 2016, Vienna Austria, https://meetingorganizer.copernicus.org/EGU2016/EGU2016-6575-1.pdf.

Bialas, R. W., & Buck, W. R. (2009). How sediment promotes narrow rifting: Application to the Gulf of California. *Tectonics*, *28*, TC4014. https://doi.org/10.1029/2008TC002394

Braun, J. (2018). A review of numerical modeling studies of passive margin escarpments leading to a new analytical expression for the rate of escarpment migration velocity. *Gondwana Research*, *53*, 209–224. http://www.sciencedirect.com/science/article/pii/S1342937X17302058 (Rifting to Passive Margins) doi: https://doi.org/10.1016/j.gr.2017.04.012

Braun, J., Deschamps, F., Rouby, D., & Dauteuil, O. (2013). Flexure of the lithosphere and the geodynamical evolution of non-cylindrical rifted passive margins: Results from a numerical model incorporating variable elastic thickness, surface processes and 3D thermal subsidence. *Tectonophysics*, *604*, 72–82. (Progress in understanding the South Atlantic margins) https://doi.org/10.1016/j.tecto.2012.09.033

Braun, J., & van der Beek, P. (2004). Evolution of passive margin escarpments: What can we learn from low-temperature thermochronology? *Journal of Geophysical Research*, *109*, F04009. https://doi.org/10.1029/2004JF000147

Braun, J., & Willett, S. D. (2013). A very efficient O(n), implicit and parallel method to solve the stream power equation governing fluvial incision and landscape evolution. *Geomorphology*, *180–181*(0), 170–179. http://dx.doi.org/10.1016/j.geomorph.2012.10.008

Brown, R. W., Summerfield, M. A., & Gleadow, A. J. W. (2002). Denudational history along a transect across the drakensberg escarpment of Southern Africa derived from apatite fission track thermochronology. *Journal of Geophysical Research*, *107*(B12), 2350. https://doi.org/10.1029/2001JB000745

Brune, S., Heine, C., Perez-Gussinye, M., & Sobolev, S. V. (2014). Rift migration explains continental margin asymmetry and crustal hyperextension. *Nature Communications*, *5*, 4014. https://doi.org/10.1038/ncomms5014

Buck, W. R. (1991). Modes of continental lithospheric extension. *Journal of Geophysical Research*, *96*(B12), 20,161–20,178. https://doi.org/10.1029/91JB01485

Buck, W. R. (1993). Effect of lithospheric thickness on the formation of high- and low-angle normal faults. *Geology*, *21*(10), 933–936. https://doi.org/10.1130/0091-7613(1993)021h0933:EOLTOTi2.3.CO;2

Buiter, S. J. H., Huismans, R. S., & Beaumont, C. (2008). Dissipation analysis as a guide to mode selection during crustal extension and implications for the styles of sedimentary basins. *Journal of Geophysical Research*, *113*, B06406. https://doi.org/10.1029/2007JB005272

Burov, E., & Poliakov, A. (2001). Erosion and rheology controls on synrift and postrift evolution: Verifying old and new ideas using a fully coupled numerical model. *Journal of Geophysical Research*, *106*(B8), 16,461–16,481. https://doi.org/10.1029/2001JB000433

Burov, E., & Poliakov, A. (2003). Erosional forcing on basin dynamics: New aspects of syn- and post-rift evolution. In niewland, d.a. (ed.) : New insights in structural interpretation and modelling. *Special Publication - Geological Society of London*, *212*, 209–224. https://doi.org/10.1144/GSL.SP.2003.212.01.14

Chamot-Rooke, N., Gaulier, J.-M., & Jestin, F. (1999). Constraints on Moho depth and crustal thickness in the Liguro-Provençal basin from a 3D gravity inversion: Geodynamic implications. *Geological Society, London, Special Publications*, *156*(1), 37–61. https://doi.org/10.1144/GSL.SP.1999.156.01.04

Choi, E., Buck, W. R., Lavier, L., & Petersen, K. D. (2013). Using core complex geometry to constrain fault strength. *Geophysical Research Letters*, *40*, 3863–3867. https://doi.org/10.1002/grl.50732

Clerc, C., Ringenbach, J.-C., Jolivet, L., & Ballard, J.-F. (2017). Rifted margins: Ductile deformation, boudinage, continentward-dipping normal faults and the role of the weak lower crust. *Gondwana Research*, *53*, 20–40. http://doi.org/10.1016/j.gr.2017.04.030

Cowie, P., & Karner, G. D. (1990). Gravity effect of sediment compaction: Examples from the north sea and the rhine graben. *Earth and Planetary Science Letters*, *99*(1–2), 141–153. http://doi.org/10.1016/0012-821X(90)90078-C

Cowie, P., Underhill, J. R., Behn, M. D., Lin, J., & Gill, C. E. (2005). Spatio-temporal evolution of strain accumulation derived from multiscale observations of late jurassic rifting in the northern north sea: A critical test of models for lithospheric extension. *Earth and Planetary Science Letters*, *234*(3-4), 401–419. https://doi.org/10.1016/j.epsl.2005.01.039

Davy, P., & Lague, D. (2009). Fluvial erosion/transport equation of landscape evolution models revisited. *Journal of Geophysical Research*, *114*, F03007. https://doi.org/10.1029/2008JF001146

Demoulin, A., Schiattarella, M., & Pedersen, V. K. (2018). Geomorphic response to active tectonics: Numerical and field-based approaches. *Earth Surface Processes and Landforms*, *43*(12), 2666–2668. https://doi.org/10.1002/esp.4397

Duretz, T., Petri, B., Mohn, G., Schmalholz, S. M., Schenker, F. L., & Müntener, O. (2016). The importance of structural softening for the evolution and architecture of passive margins. *Nature - Scientific Reports*, *6*:38704. https://doi.org/10.1038/srep38704

Erdős, Z., Huismans, R. S., van der Beek, P., & Thieulot, C. (2014). Extensional inheritance and surface processes as controlling factors of mountain belt structure. *Journal of Geophysical Research: Solid Earth*, *119*, 9042–9061. https://doi.org/10.1002/2014JB011408

Fossen, H. (2010). Extensional tectonics in the North Atlantic Caledonides: A regional view. In Law, R. D., Butler, R. W. H., Holdsworth, R. E., Krabbendam, M., & Strachan, R. A. (Eds.), *Tectonics and mountain building: The legacy of Peach and Horne*, (Vol. 335, pp. 767–793). London: The Geological Society of London. https://doi.org/10.1144/SP335.31

Fossen, H., Khani, H. F., Faleide, J. I., Ksienzyk, A. K., & Dunlap, W. J. (2016). Post-Caledonian extension in the West Norway-northern North Sea region: The role of structural inheritance. *Geological Society, London, Special Publications*, *439*, SP439–6. https://doi.org/10.1144/SP439.6

Gawthorpe, R. L., Fraser, A. J., & Collier, R. E. (1994). Sequence stratigraphy in active extensional basins: Implications for the interpretation of ancient basin-fills. *Marine and Petroleum Geology*, *11*(6), 642–658. http://doi.org/10.1016/0264-8172(94)90021-3

Gawthorpe, R. L., Jackson, C. A.-L., Young, M. J., Sharp, I. R., Moustafa, A. R., & Leppard, C. W. (2003). Normal fault growth, displacement localisation and the evolution of normal fault populations: The Hammam Faraun fault block, Suez rift, Egypt. *Journal of Structural Geology*, *25*(6), 883–895. http://doi.org/10.1016/S0191-8141(02)00088-3

Gleason, G. C., & Tullis, J. (1995). A flow law for dislocation creep of quartz aggregates determined with the molten salt cell. *Tectonophysics*, *247*(1–4), 1–23. (30 Years of Tectonophysics a Special Volume in Honour of Gerhard Oertel) http://doi.org/10.1016/0040-1951(95)00011-B

Goren, L., Willett, S. D., Herman, F., & Braun, J. (2014). Coupled numerical–analytical approach to landscape evolution modeling. *Earth Surface Processes and Landforms*, *39*(4), 522–545. Retrieved from https://onlinelibrary.wiley.com/doi/abs/10.1002/esp.3514 https://doi.org/10.1002/esp.3514

Goteti, R., Ings, S. J., & Beaumont, C. (2012). Development of salt minibasins initiated by sedimentary topographic relief. *Earth and Planetary Science Letters*, *339*, 103–116. https://doi.org/10.1016/j.epsl.2012.04.045

Hack, J. T. (1957). Studies of longitudinal profiles in Virginia and Maryland. *United States Geological Survey (USGS) Professional Paper*, *1*(294-B), 45–97. https://doi.org/10.3133/pp294B

Howard, A. D. (1994). A detachment-limited model of drainage basin evolution. *Water Resources Research*, *30*(7), 2261–2285. https://doi.org/10.1029/94WR00757

Howard, A. D., & Kerby, G. (1983). Channel changes in badlands. *Geological Society of America Bulletin*, *94*(6), 739–752. https://doi.org/10.1130/0016-7606(1983)94h739:CCIBi2.0.CO;2

Huismans, R. S., & Beaumont, C. (2002). Asymmetric lithospheric extension: The role of frictional plastic strain softening inferred from numerical experiments. *Geology*, *30*(3), 211–214. https://doi.org/10.1130/0091-7613(2002)030h0211:ALETROi2.0.CO;2

Huismans, R. S., & Beaumont, C. (2003). Symmetric and asymmetric lithospheric extension: Relative effects of frictional-plastic and viscous strain softening. *Journal of Geophysical Research*, *108*(B10), 2496. https://doi.org/10.1029/2002JB002026

Huismans, R. S., & Beaumont, C. (2008). Complex rifted continental margins explained by dynamical models of depth-dependent lithospheric extension. *Geology*, *36*(2), 163. https://doi.org/10.1130/G24231A.1

Huismans, R. S., & Beaumont, C. (2011). Depth-dependent extension, two-stage breakup and cratonic underplating at rifted margins. *Nature*, *473*(7345), 74–U85. https://doi.org/10.1038/nature09988

Huismans, R. S., & Beaumont, C. (2014). Rifted continental margins: The case for depth-dependent extension. *Earth and Planetary Science Letters*, *407*(0), 148–162. http://doi.org/10.1016/j.epsl.2014.09.032

Karato, S.-I., & Wu, P. (1993). Rheology of the upper mantle: A synthesis. *Science*, *260*(5109), 771–778. https://doi.org/10.1126/science.260.5109.771

Karner, G. D., Driscoll, N. W., & Barker, D. H. N. (2003). Syn-rift region subsidence across the West African continental margin; the role of lower plate ductile extension. In Arthur, T. J., Macgregor, D. S., & Cameron, N. (Eds.), *Petroleum geology of Africa: New themes and developing technologies*, SpecialPublications (Vol. 207, pp. 105–129). London: The Geological Society of London. https://doi.org/10.1144/GSL.SP.2003.207.6

Kooi, H., & Beaumont, C. (1994). Escarpment evolution on high-elevation rifted margins: Insights derived from a surface processes model that combines diffusion, advection, and reaction. *Journal of Geophysical Research*, *99*(B6), 12,191–12,209. https://agupubs.onlinelibrary.wiley.com/doi/abs/10.1029/94JB00047 https://doi.org/10.1029/94JB00047

Lacey, G. (1930). Stable channels in alluvium. *Minutes of Proceedings of the Institution of Civil Engineers*, *229*(4736), 259–292. https://doi.org/10.1680/imotp.1930.15592

Lague, D. (2014). The stream power river incision model: Evidence, theory and beyond. *Earth Surface Processes and Landforms*, *39*(1), 38–61. https://doi.org/10.1002/esp.3462

Lavier, L., Buck, W. R., & Poliakov, A. N. B. (2000). Factors controlling normal fault offset in an ideal brittle layer. *Journal of Geophysical Research*, *105*(B10), 23,431–23,442. https://doi.org/10.1029/2000JB900108

Lavier, L., & Manatschal, G. (2006). A mechanism to thin the continental lithosphere at magma-poor margins. *Nature*, *440*(7082), 324–328. https://doi.org/10.1038/nature04608

Lavier, L., Roger Buck, W., & Poliakov, A. N. B. (1999). Self-consistent rolling-hinge model for the evolution of large-offset low-angle normal faults. *Geology*, *27*(12), 1127–1130. https://doi.org/10.1130/0091-7613(1999)027h1127:SCRHMFi2.3.CO;2

Leeder, M. R., & Gawthorpe, R. L. (1987). Sedimentary models for extensional tilt-block/half-graben basins. In Society, G. (Ed.), *Extensional tectonics: Regional-scale processes*. (Vol. 28, pp. 171–184). London: The Geological Society of London. https://doi.org/10.1144/GSL.SP.1987.028.01.11

Maniatis, G., Kurfeß, D., Hampel, A., & Heidbach, O. (2009). Slip acceleration on normal faults due to erosion and sedimentation—Results from a new three-dimensional numerical model coupling tectonics and landscape evolution. *Earth and Planetary Science Letters*, *284*(3–4), 570–582. http://doi.org/10.1016/j.epsl.2009.05.024

Moulin, M., Aslanian, D., Olivet, J.-L., Contrucci, I., Matias, L., Géli, L., et al. (2005). Geological constraints on the evolution of the Angolan margin based on reflection and refraction seismic data (ZaïAngo Project). *Geophysical Journal International*, *162*(3), 793–810. https://doi.org/10.1111/j.1365-246X.2005.02668.x

Olive, J.-A., Behn, M. D., & Malatesta, L. C. (2014). Modes of extensional faulting controlled by surface processes. *Geophysical Research Letters*, *41*, 6725–6733. https://doi.org/10.1002/2014GL061507

Olive, J.-A., Behn, M. D., Mittelstaedt, E., Ito, G., & Klein, B. Z. (2016). The role of elasticity in simulating long-term tectonic extension. *Geophysical Journal International*, *205*(2), 728–743. https://doi.org/10.1093/gji/ggw044

Petit, C., Gunnell, Y., Gonga-Saholiariliva, N., Meyer, B., & Séguinot (2009). Faceted spurs at normal fault scarps: Insights from numerical modeling. *Journal of Geophysical Research*, *114*, B05403. https://doi.org/10.1029/2008JB005955

Prosser, S. (1993). Rift-related linked depositional systems and their seismic expression. *Geological Society, London, Special Publications*, *71*(1), 35–66. https://doi.org/10.1144/GSL.SP.1993.071.01.03

Pysklywec, R. N., & Beaumont, C. (2004). Intraplate tectonics: Feedback between radioactive thermal weakening and crustal deformation driven by mantle lithosphere instabilities. *Earth and Planetary Science Letters*, *221*(1), 275–292. http://doi.org/10.1016/S0012-821X(04)00098-6

Rigon, R., Rodriguez-Iturbe, I., Maritan, A., Giacometti, A., Tarboton, D. G., & Rinaldo, A. (1996). On Hack's law. *Water Resources Research*, *32*(11), 3367–3374. https://doi.org/10.1029/96WR02397

Roda-Boluda, D. C., & Whittaker, A. C. (2018). Normal fault evolution and coupled landscape response: Examples from the Southern Apennines, Italy. *Basin Research*, *30*(S1), 186–209. https://doi.org/10.1111/bre.12215

Ruppel, C. (1995). Extensional processes in continental lithosphere. *Journal of Geophysical Research*, *100*(B12), 24,187–24,215. https://doi.org/10.1029/95JB02955

Sacek, V., Braun, J., & van der Beek, P. (2012). The influence of rifting on escarpment migration on high elevation passive continental margins. *Journal of Geophysical Research*, *117*, B04407. https://doi.org/10.1029/2011JB008547

Salazar-Mora, C. A., Huismans, R. S., Fossen, H., & Egydio-Silva, M. (2018). The wilson cycle and effects of tectonic structural inheritance on rifted passive margin formation. *Tectonics*, *37*, 3085–3101. https://doi.org/10.1029/2018TC004962

Savenije, H. H. G. (2003). The width of a bankfull channel; Lacey's formula explained. *Journal of Hydrology*, *276*(1–4), 176–183. http://doi.org/10.1016/S0022-1694(03)00069-6

Schlische, R. W. (1991). Half-graben basin filling models: New constraints on continental extensional basin development. *Basin Research*, *3*(3), 123–141. https://doi.org/10.1111/j.1365-2117.1991.tb00123.x

Schlische, R. W. (2003). Progress in understanding the structural geology, basin evolution, and tectonic history of the eastern North American Rift System. In Le Tourneau, P. M., & Olsen, P. E. (Eds.), *The Great Rift Valleys of Pangea in Eastern North America-Volume One: Tectonics, Structure, and Volcanism*, chapter 4, Columbia University press. (Vol. 1, pp. 21–64). New York. https://doi.org/10.7312/leto11162-003

Seranne, M., & Seguret, M. (1987). The Devonian basins of western Norway: Tectonics and kinematics of an extending crust. *Geological Society, London, Special Publications*, *28*(1), 537–548. https://doi.org/10.1144/GSL.SP.1987.028.01.35

Steer, P., Cattin, R., Lavé, J., & Godard, V. (2011). Surface Lagrangian remeshing: A new tool for studying long term evolution of continental lithosphere from 2D numerical modelling. *Computers and Geosciences*, *37*(8), 1067–1074. http://doi.org/10.1016/j.cageo.2010.05.023

Steer, P., Simoes, M., Cattin, R., & Shyu, J. B. H. (2014). Erosion influences the seismicity of active thrust faults. *Nature Communications*, *5*, 5564. https://doi.org/10.1038/ncomms6564

Stolar, D. B., Willett, S. D., & Roe, G. H. (2006). Climatic and tectonic forcing of a critical orogen. *Geological Society of America Special Papers*, *398*, 241–250. https://doi.org/10.1130/2006.2398(14)

Strak, V., Dominguez, S., Petit, C., Meyer, B., & Loget, N. (2011). Interaction between normal fault slip and erosion on relief evolution: Insights from experimental modelling. *Tectonophysics*, *513*(1–4), 1–19. http://doi.org/10.1016/j.tecto.2011.10.005

Svartman Dias, A. E., Lavier, L., & Hayman, N. W. (2015). Conjugate rifted margins width and asymmetry: The interplay between lithospheric strength and thermomechanical processes. *Journal of Geophysical Research: Solid Earth*, *120*, 8672–8700. https://doi.org/10.1002/2015JB012074

Tenzer, R., & Gladkikh, V. (2014). Assessment of density variations of marine sediments with ocean and sediment depths. *The Scientific World Journal*, *2014*(Article ID 823296), 9p.https://doi.org/10.1155/2014/823296

Tetreault, J. L., & Buiter, S. J. H. (2018). The influence of extension rate and crustal rheology on the evolution of passive margins from rifting to break-up. *Tectonophysics*, *746*, 155–172. (Understanding geological processes through modelling - A Memorial Volume honouring Evgenii Burov) https://doi.org/10.1016/j.tecto.2017.08.029

Thieulot, C. (2011). Fantom: Two- and three-dimensional numerical modelling of creeping flows for the solution of geological problems. *Physics of the Earth and Planetary Interiors*, *188*(1–2), 47–68. http://doi.org/10.1016/j.pepi.2011.06.011

Thieulot, C., Steer, P., & Huismans, R. S. (2014). Three-dimensional numerical simulations of crustal systems undergoing orogeny and subjected to surface processes. *Geochemistry, Geophysics, Geosystems*, *15*, 4936–4957. https://doi.org/10.1002/2014GC005490

Tucker, G. E., & Whipple, K. X. (2002). Topographic outcomes predicted by stream erosion models: Sensitivity analysis and intermodel comparison. *Journal of Geophysical Research*, *107*(B9), 2179. https://doi.org/10.1029/2001JB000162

van Balen, R. T., van der Beek, P. A., & Cloetingh, S. A. P. L. (1995). The effect of rift shoulder erosion on stratal patterns at passive margins: Implications for sequence stratigraphy. *Earth and Planetary Science Letters*, *134*(3–4), 527–544. http://doi.org/10.1016/0012-821X(95)98955-L

van der Beek, P., Summerfield, M. A., Braun, J., Brown, R. W., & Fleming, A. (2002). Modeling postbreakup landscape development and denudational history across the Southeast African (drakensberg escarpment) margin. *Journal of Geophysical Research*, *107*(B12), 11–18. https://doi.org/10.1029/2001JB000744

Whipple, K. X. (2009). The influence of climate on the tectonic evolution of mountain belts. *Nature Geoscience*, *2*, 97–104. https://doi.org/10.1038/ngeo413

Whipple, K. X., Hancock, G. S., & Anderson, R. S. (2000). River incision into bedrock: Mechanics and relative efficacy of plucking, abrasion, and cavitation. *Geological Society of America Bulletin*, *112*(3), 490–503. https://doi.org/10.1130/0016-7606(2000)112h490:RIIBMAi2.0.CO;2

Whipple, K. X., Kirby, E, & Brocklehurst, S. H. (1999). Geomorphic limits to climate-induced increases in topographic relief. *Nature*, *401*(6748), 39–43. https://doi.org/10.1038/43375

Whipple, K. X., & Tucker, G. E. (1999). Dynamics of the stream-power river incision model: Implications for height limits of mountain ranges, landscape response timescales, and research needs. *Journal of Geophysical Research*, *104*(B8), 17,661–17,674. https://doi.org/10.1029/1999JB900120

Willett, S. D. (1992). Dynamic and kinematic growth and change of a Coulomb wedge. In McClay, K. R. (Ed.), *Thrust tectonics*. Dordrecht: Springer Netherlands, pp. 19–31. https://doi.org/10.1007/978-94-011-3066-0

Willett, S. D. (1999). Orogeny and orography: The effects of erosion on the structure of mountain belts. *Journal of Geophysical Research*, *104*(B12), 28,957–28,981. https://doi.org/10.1029/1999JB900248

Willett, S. D. (2010). Erosion on a line. *Tectonophysics*, *484*(1–4), 168–180. (Quantitative modelling of geological processes) http://doi.org/10.1016/j.tecto.2009.09.011

Withjack, M. O., & Schlische, R. W. (2005). A review of tectonic events on the passive margin of eastern north america. In Post, P. J., Rosen, N. C., Olson, D. L., Palmes, S. L., Lyons, K. T., & Newton, G. B. (Eds.), *Petroleum systems of divergent continental margin basins: 25th bob s. Perkins research conference*. (Vol. 25, pp. 203–235). Houston: Gulf Coast Section of SEPM. https://doi.org/10.5724/gcs.05.25.0203

Withjack, M. O., Schlische, R. W., & Olsen, P. E. (1998). Diachronous rifting, drifting, and inversion on the passive margin of central eastern North America: An analog for other passive margins. *AAPG Bulletin-American Association of Petroleum Geologists*, *82*(5, A), 817–835, https://doi.org/10.1306/1d9bc60b-172d-11d7-8645000102c1865d

Wu, G., & Lavier, L.The effects of lower crustal strength and preexisting midcrustal shear zones on the formation of continental core complexes and low-angle normal faults. *Tectonics*, *35*, 2195–2214. https://doi.org/10.1002/2016TC004245

Wu, G., Lavier, L., & Choi, E. (2015). Modes of continental extension in a crustal wedge. *Earth and Planetary Science Letters*, *421*, 89–97. http://doi.org/10.1016/j.epsl.2015.04.005

Yuan, X. P., Braun, J., Guerit, L., Rouby, D., & Cordonnier, G. (2019). A new efficient method to solve the stream power law model taking into account sediment deposition. *Journal of Geophysical Research: Earth Surface*, *124*, 1346–1365. https://agupubs.onlinelibrary.wiley.com/doi/abs/10.1029/2018JF004867 https://doi.org/10.1029/2018JF004867